Lithos 232 (2015) 375–394

Contents lists available at ScienceDirect

Lithos

journal homepage: www.elsevier.com/locate/lithos

Insights into the behaviour of S, F, and Cl at Santiaguito Volcano, Guatemala, from apatite and glass

Jeannie A.J. Scott [a], Madeleine C.S. Humphreys [a,b,*], Tamsin A. Mather [a], David M. Pyle [a], Michael J. Stock [a]

[a] Department of Earth Sciences, University of Oxford, South Parks Road, Oxford, OX1 3AN, UK
[b] Department of Earth Sciences, Durham University, Science Labs, Durham, DH1 3LE, UK

ARTICLE INFO

Article history:
Received 14 August 2014
Accepted 15 July 2015
Available online 23 July 2015

Keywords:
Santiaguito
Apatite
Pre-eruptive volatile concentrations
Gas emissions
Degassing
Petrologic method

ABSTRACT

The mineral apatite can incorporate all of the major magmatic volatile species into its structure. Where melt inclusions are not available, magmatic apatite may therefore represent an opportunity to quantify volatile concentrations in the pre-eruptive melt. We analysed apatites and matrix glasses from andesites and dacites erupted from Santiaguito Volcano, Guatemala, between the 1920s and 2002. X-ray mapping shows complex zoning of sulphur in the apatite grains, but typically with sulphur-rich cores and sulphur-poor rims. Apatite microphenocrysts are enriched in F and depleted in Cl relative to inclusions. Matrix glasses are dacite to rhyolite and contain low F but up to 2400 ppm Cl. Overall, the data are consistent with progressive depletion of Cl in the most evolved melts due to crystallisation and degassing. In the absence of pristine melt inclusions, we used apatite, together with published partitioning data, to reconstruct the likely volatile contents of the pre-eruptive melt, and hence estimate long-term average gas emissions of SO_2, HF and HCl for the ongoing eruption. The data indicate time-averaged SO_2 emissions of up to 157 tonnes/day, HCl of 74–1382 tonnes/day and up to 196 tonnes/day HF. Apatite may provide a useful measure of long-term volatile emissions at volcanoes where direct emissions measurements are unavailable, or for comparison with intermittent gas sampling methods. However, significant uncertainty remains regarding volatile distribution coefficients for apatite, and their variations with temperature and pressure.

1. Introduction

The exsolution of dissolved magmatic volatiles into bubbles during magma ascent and eruption is one of the most important processes affecting the physical properties of any volcanic system. Whereas H_2O and CO_2 are the most important volatiles by volume, S, F and Cl can have significant environmental consequences on a local to global scale, with relevance to atmospheric chemistry, human health, and ecology (e.g. Allen et al., 2000; Martin et al., 2009; Robock, 2000). Constraining the fluxes of these volatiles is an important means to assess the current and past impact of volcanic activity on the Earth's surface environment. In the absence of direct measurements of gas emissions, the volatile contents of melt inclusions, trapped in phenocrysts and isolated at depth, are routinely used to infer pre-eruptive melt volatile concentrations (e.g. Bouvier et al., 2008; Edmonds et al., 2001; Humphreys et al., 2008; Wallace, 2005). Comparison of these pre-eruptive volatile concentrations with those preserved in the matrix glass gives a petrologic estimate of volatiles degassed during volcanic eruptions (Devine et al., 1984; Thordarson et al., 1996).

However, in some magmas, melt inclusions may only be present in phases that are liable to leak or degas, or they may be present but too small for analysis, or have undergone devitrification or significant post-entrapment modification. In such cases, an alternative method for assessment of pre-eruptive volatile contents is required. Here we explore and evaluate the potential use of apatite in place of melt inclusions, to infer pre-eruptive concentrations of S, F and Cl in the magmatic liquid at Santiaguito volcano, Guatemala, commenting on the advantages and limitations of the method. This work builds on previous studies, for example at Huaynaputina, Peru (Dietterich and de Silva, 2010) and Irazú volcano, Costa Rica (Boyce and Hervig, 2009). We use the data to infer pre-eruptive volatile concentrations in magmas erupted from Santiaguito volcano, and hence estimate the time-averaged gas emissions of this long-lived, but poorly monitored, volcanic dome complex.

2. Geological background and petrology

Activity at the silicic lava dome complex of Santiaguito, Guatemala, began in 1922 and continues at the time of writing (2015). The dome sits on the shoulder of the much older Santa María volcanic edifice, which in 1902 was the site of a major bimodal explosive eruption, dominated by dacite pumice. Activity at the Santiaguito edifice is

* Corresponding author at: Department of Earth Sciences, Durham University, Science Labs, Durham, DH1 3LE, UK.
E-mail address: madeleine.humphreys@durham.ac.uk (M.C.S. Humphreys).

http://dx.doi.org/10.1016/j.lithos.2015.07.004

characterized by extrusion of lava domes and flows, with regular explosive release of gas and ash (Bluth and Rose, 2004; Escobar Wolf et al., 2010; Rose, 1972, 1987), and substantial passive degassing between explosions (Holland et al., 2011). Persistent cloud cover, challenging terrain, and the explosive nature of the volcanic activity have limited the measurement of volatile emissions using satellite- or ground-based remote sensing methods or direct techniques (Santa María Volcano Observatory written records; Holland et al., 2011; Rodriguez et al., 2004). However, previous work indicates that the effusive eruption of Santiaguito should result in significant halogen output in the volcanic plume as a result of open-system degassing (Balcone-Boissard et al., 2010; Villemant et al., 2003).

2.1. Petrology of Santa María – Santiaguito

The chemical and petrological features of the Santa María – Santiaguito magmas have previously been described (Jicha et al., 2010; Rose, 1972, 1987; Scott et al., 2012, 2013; Singer et al., 2011, 2014), and we summarize the main points below. The Santa María magmas are typically basaltic andesite, but span a wide range of compositions from 51 wt% to 69 wt% SiO_2 (e.g. Rose, 1987). The earliest magmas erupted from Santiaguito itself were similar in composition to the 1902 pumice from Santa María (Rose 1972; Singer et al., 2011). Santiaguito eruptive products are typically porphyritic andesites to dacites (62–66 wt% SiO_2) with ~20–30 vol% plagioclase phenocrysts and ~5 vol% orthopyroxene + Fe-Ti oxides + augite ± olivine ± amphibole. The plagioclase phenocrysts commonly display one or more resorption surfaces with clear, euhedral rims; in many of the more recent samples the majority of the plagioclase crystals show severe resorption textures and a network of large, irregular, devitrified melt inclusions in the core. Accessory minerals include apatite, cristobalite, and pyrrhotite, the latter as inclusions in titanomagnetite phenocrysts. The groundmass consists of matrix glass, euhedral plagioclase, and equant to feathery microlites of orthopyroxene and titanomagnetite.

Glomerocrysts of plagioclase ± orthopyroxene ± olivine are common and contain large pools of interstitial glass (Fig. 1). These glomerocrysts preserve asymmetry at plagioclase-plagioclase-melt boundaries (Fig. 1d), due to the development of curved plagioclase-melt interfaces, rather than simple impingement textures with planar crystal surfaces. This suggests changes in the differential growth rates between different plagioclase crystallographic axes. These textures are similar to those observed in slowly cooling gabbroic cumulates (Holness et al., 2012) and, by analogy, suggests very slow growth. We therefore infer that these glomerocrysts may represent fragments of disrupted mush that would have gone on to form solid plutonic rocks at depth. Matrix and glomerocryst glass compositions range from ~66 to ~76 wt% SiO_2 and are similar to the compositions of melt inclusions (64.5–73.5 wt% SiO_2, Singer et al., 2014).

Thermobarometry based on amphibole phenocryst compositions suggests magma crystallisation temperatures of ~940–980 °C (±22 °C) at moderately oxidising conditions in the region of NNO + 0.5 to NNO + 2 (Scott et al., 2012; Singer et al., 2014), and this agrees with observed maximum surface eruption temperatures (850–950 °C, Sahetapy-Engel et al., 2004). Fe-Ti oxide compositions from the 1902 eruption give temperatures of 860–885 °C for the dacite and 925–1040 °C for the andesite (Singer et al., 2014). Petrological and geochemical studies of Santiaguito show that the lavas have become more mafic with time since the eruption recommenced in 1922 (Escobar Wolf et al., 2010; Scott et al., 2013).

Apatite is present in all samples as microphenocrysts and/or as inclusions within phenocryst phases (typically clinopyroxene), indicating early apatite saturation in the melt (Fig. 2). Some crystals are fully included within the host mineral while others are partly open to the matrix (Fig. 2), permitting variable degrees of equilibration with the host melt. The common occurrence of apatites included in pyroxene may be related to synneusis. The inclusions are equant and thus clearly distinct from the acicular quench crystals commonly observed in plagioclase phenocrysts elsewhere (e.g. Bacon, 1986; Wyllie et al., 1962), which are thought to form as a result of growth from a melt boundary

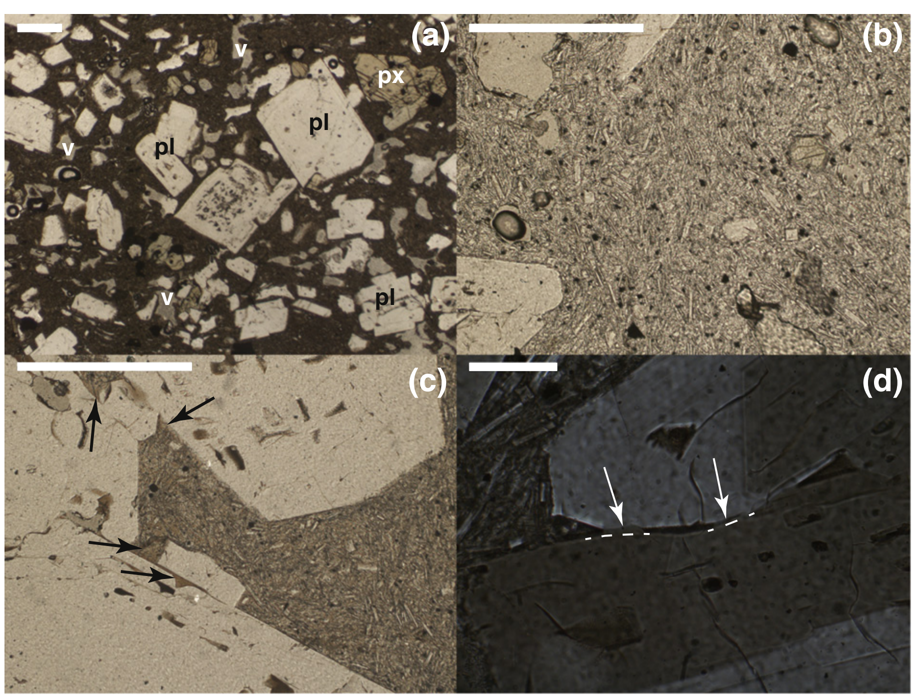

Fig. 1. Photomicrographs of typical dome rocks from Santiaguito Volcano. (a) Porphyritic texture with abundant plagioclase phenocrysts (pl), pyroxene (px) and vesicles (v). (b) Typical groundmass texture with abundant euhedral microlites of plagioclase, pyroxenes and oxides. (c) Matrix glass (arrowed) can be found as small patches and embayments near the margins of glomerocrysts. (d) Cumulate-type grain boundary textures are found in some plagioclase glomerocrysts. This is manifest as marked asymmetry of plagioclase-plagioclase junctions, resulting in small filaments of feldspar (arrowed; expected grain boundary marked with dashed line) joining adjacent grains of the glomerocryst. This is similar to that observed in gabbros (Holness et al., 2012) and suggests very slow cooling. Dark blebs are partially devitrified melt inclusions. Scale bar is 1 mm in all images except d (100 μm).

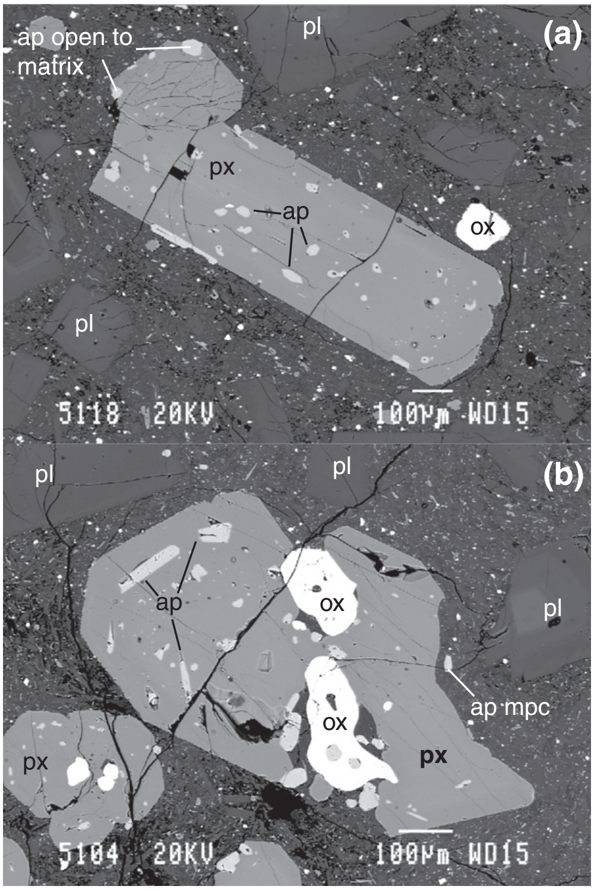

Fig. 2. Back-scattered electron SEM images showing typical occurrences of apatite in dome rocks from Santiaguito Volcano, both as abundant inclusions within pyroxene (px) phenocrysts or crystal clots of pyroxene with oxides (ox), and as microphenocrysts in the matrix. Some of the inclusions are open to the matrix (a). In (a) many of the apatite inclusions themselves contain tiny melt inclusions that appear as dark dots.

layer at the crystal-melt interface. Apatite microphenocrysts are texturally similar to those present as inclusions; their timing of crystallisation relative to the inclusions is unclear but we assume that the microphenocrysts were at least open to significant equilibration with the host melt. The apatites are relatively large, up to 150 µm in length, which is typically significantly larger than groundmass plagioclase, orthopyroxene and titanomagnetite microlites.

2.2. Magma supply and fractionation

There is clear evidence of open-system processes at Santa-María – Santiaguito, with a large range of magma compositions erupted, from basaltic andesite to dacite. The deep supply of magma is dominated by hybrid basaltic andesites, fractionating amphibole in the deep crust and assimilating crustal material to form more silicic compositions (Jicha et al., 2010; Singer et al., 2011, 2014). The shallow magmatic system is thought to comprise an elongate, perhaps chemically stratified magma storage region (Rose, 1972; Scott et al., 2013), in which magmas decompress, degas and crystallise. There is clear evidence for mixing of more mafic magmas with the dacites (Singer et al., 2011, 2014) including reversely zoned plagioclase and the presence of mafic enclaves, as well as plutonic material.

2.3. Samples studied

Our dataset comes from analysis of 24 samples from Santiaguito, representing many of the dome and flow units of the complex, and dating from the 1920s to 2002, as reported in Scott et al. (2012, supplementary table A) and in Scott (2012). We consider in detail the glass dataset of Scott et al. (2013, supplementary table D) together with some new glass analyses and a large dataset of apatite compositions.

3. Analytical methods

Mineral analyses were obtained by electron probe microanalysis on a four-spectrometer JEOL JXA-8600 electron microprobe in the Research Laboratory for Archaeology and the History of Art, University of Oxford. For apatite, long exposure to the electron beam results in sample damage in the form of volatile migration; this effect is strongly anisotropic and is most significant for halogen analyses conducted parallel to the c-axis of the crystal (e.g. Goldoff et al., 2012; Stock et al., 2015; Stormer et al., 1993). Selection of analytical beam conditions is a trade-off between the accuracy of halogen concentrations (needing a lower accelerating voltage and beam current to minimise electron beam-induced migration) and the precision of heavy and minor element analyses (e.g. Fe, Mn, requiring at least 15 kV accelerating voltage and higher beam currents, Stock et al., 2015). For most analyses, we used relatively short (30s) peak count times for all elements, a 15 kV accelerating voltage and a 15 nA defocused (5 µm) beam, with F, Cl and P analysed first. We found no discernible difference between analyses of grains with different crystallographic orientations, within the uncertainty of our analyses and the variance of the crystal population. We also analysed a subset of analyses using a 10 nA, 5 µm electron beam and these were consistent with the lower-F compositions of those analysed at 15 nA, albeit with slightly larger analytical uncertainties (see Table 1). For these analyses, 120 s peak counting times were used for F, Cl and S. Analyses with totals <95 wt% were excluded, as were those that did not give good stoichiometric formulae. Wilberforce and Durango apatite, oriented both parallel and perpendicular to the electron beam, were used as secondary standards to check the accuracy of the analyses. These did show slightly higher F contents for crystals oriented with the c-axis parallel to the electron beam, as demonstrated previously (e.g. Stormer et al., 1993). The sulphur peak position was checked prior to analysis and S was calibrated using $BaSO_4$. Analytical precision was typically better than 0.2 wt% for F, 0.13 wt% for Cl and ~500 ppm for S, and is given in Table 1.

We also performed element mapping on eighteen apatites from five different samples, including microphenocrysts and inclusions in pyroxene, using a JEOL JXA-8800 electron microprobe at the University of Oxford with a 15 kV, 15 nA electron beam. These crystals did not subsequently undergo quantitative analysis. Mapping used WDS for S, Cl, and F, and simultaneous EDS for all other elements (Al, Ca, Fe, K, Na, P, Si, Ti). Resulting images were 256 by 256 pixels, with a count time of ~45 microseconds per pixel.

For glasses, we used the existing matrix glass dataset of Scott et al. (2013) (see Table 2). We also analysed a small set of interstitial glasses from the glomerocrysts, using a 15 kV, 6 nA defocused (10 µm) beam, with alkalis analysed first to avoid electron-beam damage (e.g. Devine et al., 1995; Humphreys et al., 2006a). Peak counting times were 90s for F and S, 60s for Cl, 80s for Mg, 12 s for Na and 30s for all other elements. The sulphur peak position was checked prior to analysis and calibrated using $BaSO_4$.

4. Results

4.1. Apatite compositions

Apatites from Santiaguito are typically fluorapatite with ~0.6–1.5 wt% Cl (Table 1). Minor elements include ~0.2–1.2 wt% FeO, 0.1–0.35 wt% MgO, 0.1–0.5 wt% MnO, up to ~0.7 wt% SiO_2, and up to ~4000 ppm sulphur. There are no significant compositional differences between apatites in andesitic samples and those in the dacites, or between different phases of the eruption. The volatile contents of the

Table 1
Electron microprobe analyses of apatite. Analyses were taken in the centre of each 2D grain section unless otherwise specified.

Point identifier	Sample number		Analytical setup	Unit	Vent	Sample type		SiO_2	FeO	MnO	MgO	CaO	P_2O_5	SO_3
12	SG-09-32	Inclusion	15 nA, 30s on peak	RmB	Monje	Dome		0.17	0.70		0.13	54.32	40.97	0.40
23	SG-09-32	Inclusion	15 nA, 30s on peak	RmB	Monje	Dome		0.14	0.61		0.20	53.52	41.11	0.22
32	SG-09-32	Inclusion	15 nA, 30s on peak	RmB	Monje	Dome		0.24	0.56		0.21	53.53	40.61	0.56
65	2006-69	Inclusion	15 nA, 30s on peak	-	Caliente	Bomb		0.13	0.45		0.24	53.67	39.50	0.44
70	2006-69	Inclusion	15 nA, 30s on peak	-	Caliente	Bomb		0.20	0.74		0.23	53.86	40.99	0.33
81	2006-69	Inclusion	15 nA, 30s on peak	-	Caliente	Bomb		0.16	0.75		0.25	53.32	39.57	0.45
83	2006-69	Inclusion	15 nA, 30s on peak	-	Caliente	Bomb		0.10	0.57		0.22	53.70	41.58	0.18
84	2006-69	Inclusion	15 nA, 30s on peak	-	Caliente	Bomb		0.09	0.47		0.24	54.14	39.33	0.22
100	SG-09-24	Inclusion	15 nA, 30s on peak	-	Caliente	Collapse		0.18	0.66		0.22	53.02	40.84	0.53
102	SG-09-24	Inclusion	15 nA, 30s on peak	-	Caliente	Collapse		0.13	0.89		0.24	53.36	40.96	0.29
103	SG-09-24	Inclusion	15 nA, 30s on peak	-	Caliente	Collapse		0.14	0.49		0.21	53.32	40.36	0.37
104	SG-09-24	Inclusion	15 nA, 30s on peak	-	Caliente	Collapse		0.11	0.42		0.14	53.64	39.93	0.23
108	SG-09-24	Inclusion	15 nA, 30s on peak	-	Caliente	Collapse		0.29	0.21		0.20	53.61	40.32	0.53
109	SG-09-24	Inclusion	15 nA, 30s on peak	-	Caliente	Collapse		0.20	0.87		0.23	53.34	39.83	0.34
125	SG-09-24	Inclusion	15 nA, 30s on peak	-	Caliente	Collapse		0.27	0.81		0.22	53.15	40.11	0.62
127	SG-09-24	Inclusion	15 nA, 30s on peak	-	Caliente	Collapse		0.14	0.44		0.24	53.89	41.12	0.23
104	SG-09-01	Inclusion	15 nA, 30s on peak	RcM1	Caliente	Flow		0.24	0.94	0.15	0.29	53.84	39.32	0.45
117	SG-09-01	Inclusion	15 nA, 30s on peak	RcM1	Caliente	Flow		0.23	0.74	0.19	0.26	53.63	39.10	0.44
119	SG-09-01	Inclusion	15 nA, 30s on peak	RcM1	Caliente	Flow		0.25	1.04	0.24	0.28	53.27	39.54	0.42
136	SG-09-01	Inclusion	15 nA, 30s on peak	RcM1	Caliente	Flow		0.15	0.94	0.54	0.33	53.16	39.02	0.30
145	SG-09-07	Inclusion	15 nA, 30s on peak	RcM3	Caliente	Flow		0.33	0.45	0.19	0.30	54.00	39.30	0.66
168	SG-09-07	Inclusion	15 nA, 30s on peak	RcM3	Caliente	Flow		0.28	0.31	0.18	0.25	54.93	38.97	0.30
232	SG-09-04	Inclusion	15 nA, 30s on peak	RcL	Caliente	Flow		0.35	0.82	0.13	0.31	54.01	39.27	0.37
34172_a1_2	SG-09-05	Inclusion	10 nA, 120 s on peak	RcL	Caliente	Flow		0.18	0.55	0.24	0.16	52.93	40.26	0.55
34172_a1_3	SG-09-05	Inclusion (rim)	10 nA, 120 s on peak	RcL	Caliente	Flow		0.13	0.84	0.21	0.19	52.82	41.09	0.35
34172_a1_4	SG-09-05	Inclusion	10 nA, 120 s on peak	RcL	Caliente	Flow		0.32	1.18	0.38	0.24	52.19	41.07	0.44
34172_a1_5	SG-09-05	Inclusion	10 nA, 120 s on peak	RcL	Caliente	Flow		0.38	0.98	0.28	0.23	53.11	40.49	0.72
34172_a1_7	SG-09-05	Inclusion	10 nA, 120 s on peak	RcL	Caliente	Flow		0.28	0.95	0.19	0.18	52.59	40.93	0.54
34172_a1_9	SG-09-05	Inclusion	10 nA, 120 s on peak	RcL	Caliente	Flow		0.69	0.98	0.21	0.21	52.83	40.13	1.01
34172_a3_3	SG-09-05	Inclusion	10 nA, 120 s on peak	RcL	Caliente	Flow		0.21	0.87	0.20	0.16	53.80	41.42	0.28
34172_a3_7	SG-09-05	Inclusion	10 nA, 120 s on peak	RcL	Caliente	Flow		0.35	0.80	0.10	0.17	52.93	40.85	0.72
34172_a4_1	SG-09-05	Inclusion	10 nA, 120 s on peak	RcL	Caliente	Flow		0.28	0.39	0.18	0.14	52.86	39.97	0.50
133	1121-67	Inclusion	15 nA, 30s on peak	Rb	Brujo	Dome		0.23	0.69		0.24	53.59	39.66	0.62
134	1121-67	Inclusion	15 nA, 30s on peak	Rb	Brujo	Dome		0.22	0.60		0.26	53.23	38.49	0.37
137	1121-67	Inclusion	15 nA, 30s on peak	Rb	Brujo	Dome		0.27	0.78		0.22	53.32	40.57	0.74
138	1121-67	Inclusion	15 nA, 30s on peak	Rb	Brujo	Dome		0.10	0.64		0.23	54.20	40.84	0.31
139	1121-67	Inclusion	15 nA, 30s on peak	Rb	Brujo	Dome		0.22	0.62		0.20	53.06	40.34	0.43
140	1121-67	Inclusion	15 nA, 30s on peak	Rb	Brujo	Dome		0.21	0.73		0.23	54.25	39.75	0.64
144	1121-67	Inclusion	15 nA, 30s on peak	Rb	Brujo	Dome		0.22	0.64		0.21	53.49	40.80	0.46
147	1121-67	Inclusion	15 nA, 30s on peak	Rb	Brujo	Dome		0.10	0.75		0.23	54.10	40.77	0.29
148	1121-67	Inclusion	15 nA, 30s on peak	Rb	Brujo	Dome		0.16	0.92		0.27	53.42	41.09	0.23
129	550-67	Inclusion	15 nA, 30s on peak	RbC	Brujo	Flow		0.14	0.72	0.20	0.26	54.65	39.29	0.15
8	SG-09-30	Inclusion	15 nA, 30s on peak	RbC	Brujo	Flow		0.11	0.76	0.34	0.25	54.05	40.46	0.23
9	SG-09-30	Inclusion	15 nA, 30s on peak	RbC	Brujo	Flow		0.09	0.74	0.31	0.24	53.26	40.51	0.17
12	SG-09-30	Inclusion	15 nA, 30s on peak	RbC	Brujo	Flow		0.23	0.86	0.42	0.23	53.84	40.12	0.39
35	SG-09-30	Inclusion	15 nA, 30s on peak	RbC	Brujo	Flow		0.21	0.79	0.11	0.21	54.30	39.68	0.35
41	SG-09-30	Inclusion	15 nA, 30s on peak	RbC	Brujo	Flow		0.23	0.77	0.22	0.24	53.97	40.91	0.38
42	SG-09-30	Inclusion	15 nA, 30s on peak	RbC	Brujo	Flow		0.19	0.81	0.19	0.27	53.86	39.81	0.36
167	SG-09-38	Inclusion	15 nA, 30s on peak	ReA	Mitad	Flow		0.33	0.74	0.17	0.24	53.88	40.36	0.41
80	2003-69	Inclusion	15 nA, 30s on peak	Re	Mitad	Dome		0.10	0.57	0.22	0.26	54.35	39.70	0.22
6	2002-69	Inclusion	15 nA, 30s on peak	Re	Mitad	Dome		0.25	0.81		0.22	53.57	39.92	0.44
21	SG-09-36	Inclusion	15 nA, 30s on peak	ReA	Mitad	Flow		0.15	0.73	0.22	0.22	53.84	38.92	0.34
							Mean	*0.21*	*0.71*	*0.23*	*0.23*	*53.59*	*40.19*	*0.41*
							stdev	*0.10*	*0.19*	*0.10*	*0.04*	*0.54*	*0.75*	*0.17*
							Median	*0.21*	*0.74*	*0.20*	*0.23*	*53.60*	*40.29*	*0.38*

Point identifier	Sample number			Unit	Vent	Type	SiO_2	FeO	MnO	MgO	CaO	P_2O_5	SO_3
58	2006-69	Open to matrix	15 nA, 30s on peak	-	Caliente	Bomb	0.16	0.54		0.23	54.05	39.93	0.28
64	2006-69	Open to matrix	15 nA, 30s on peak	-	Caliente	Bomb	0.22	0.71		0.25	53.90	40.42	0.47
66	2006-69	Open to matrix	15 nA, 30s on peak	-	Caliente	Bomb	0.24	0.93		0.19	53.73	40.62	0.25
68	2006-69	Open to matrix	15 nA, 30s on peak	-	Caliente	Bomb	0.19	0.68		0.19	53.83	39.92	0.35
69	2006-69	Open to matrix	15 nA, 30s on peak	-	Caliente	Bomb	0.10	0.60		0.26	54.24	38.75	0.20
71	2006-69	Open to matrix	15 nA, 30s on peak	-	Caliente	Bomb	0.26	0.82		0.23	53.92	39.99	0.55
74	2006-69	Open to matrix	15 nA, 30s on peak	-	Caliente	Bomb	0.09	0.32		0.25	54.39	41.07	0.12
85	2006-69	Open to matrix	15 nA, 30s on peak	-	Caliente	Bomb	0.28	0.68		0.26	54.48	41.23	0.32
99	SG-09-24	Open to matrix	15 nA, 30s on peak	-	Caliente	Collapse	0.33	0.56		0.16	52.06	36.64	0.26
124	SG-09-24	Open to matrix	15 nA, 30s on peak	-	Caliente	Collapse	0.17	1.24		0.29	54.01	40.73	0.24
141	1121-67	Open to matrix	15 nA, 30s on peak	Rb	Brujo	Dome	0.18	0.66		0.23	54.16	40.23	0.43
145	1121-67	Open to matrix	15 nA, 30s on peak	Rb	Brujo	Dome	0.17	0.35		0.23	54.05	41.43	0.27
146	1121-67	Open to matrix	15 nA, 30s on peak	Rb	Brujo	Dome	0.25	0.73		0.19	53.63	40.51	0.48
150	1121-67	Open to matrix	15 nA, 30s on peak	Rb	Brujo	Dome	0.38	0.60		0.20	53.23	39.73	0.34
151	1121-67	Open to matrix	15 nA, 30s on peak	Rb	Brujo	Dome	0.28	0.82		0.22	52.95	40.47	0.45
155	1121-67	Open to matrix	15 nA, 30s on peak	Rb	Brujo	Dome	0.24	1.09		0.24	54.01	40.64	0.49
157	1121-67	Open to matrix	15 nA, 30s on peak	Rb	Brujo	Dome	0.20	0.73		0.26	53.91	40.77	0.48

F	Cl	Total	O = F,Cl	S ppm	stdev F (wt%)	stdev Cl (wt%)	stdev S (ppm)	Si	Fe	Ca	Mg	Mn	S	P	F	Cl	OH*
1.38	1.40	99.47	0.90	1592	0.16	0.14	544	0.03	0.10	10.07	0.03		0.05	6.00	0.75	0.41	0.834
1.88	1.00	98.68	1.02	899	0.19	0.12	408	0.02	0.09	9.95	0.05		0.03	6.04	1.03	0.29	0.673
1.32	1.05	98.08	0.79	2254	0.16	0.12	646	0.04	0.08	10.02	0.05		0.07	6.01	0.73	0.31	0.962
1.19	1.17	96.80	0.77	1752	0.15	0.13	569	0.02	0.07	10.24	0.06		0.06	5.96	0.67	0.35	0.975
2.52	1.01	99.87	1.29	1327	0.22	0.12	495	0.03	0.11	9.91	0.06		0.04	5.96	1.37	0.29	0.337
1.08	1.36	96.94	0.76	1808	0.14	0.14	577	0.03	0.11	10.17	0.07		0.06	5.96	0.61	0.41	0.984
1.34	1.07	98.76	0.81	714	0.16	0.12	363	0.02	0.08	9.97	0.06		0.02	6.10	0.74	0.31	0.949
1.31	1.06	96.85	0.79	887	0.16	0.12	404	0.02	0.07	10.36	0.06		0.03	5.94	0.74	0.32	0.939
1.22	1.31	97.98	0.81	2133	0.15	0.13	627	0.03	0.10	9.93	0.06		0.07	6.04	0.68	0.39	0.937
2.41	1.44	99.72	1.34	1165	0.21	0.14	464	0.02	0.13	9.85	0.06		0.04	5.97	1.32	0.42	0.263
1.16	1.32	97.37	0.79	1483	0.15	0.13	523	0.03	0.07	10.08	0.06		0.05	6.03	0.65	0.39	0.956
1.61	1.54	97.63	1.03	902	0.17	0.15	408	0.02	0.06	10.16	0.04		0.03	5.97	0.90	0.46	0.636
2.59	1.18	98.93	1.36	2122	0.22	0.13	626	0.05	0.03	9.95	0.05		0.07	5.91	1.42	0.35	0.234
1.45	1.40	97.67	0.93	1366	0.16	0.14	502	0.03	0.13	10.10	0.06		0.05	5.96	0.81	0.42	0.770
1.27	1.52	97.98	0.88	2483	0.15	0.14	677	0.05	0.12	10.00	0.06		0.08	5.96	0.70	0.45	0.845
1.69	1.28	99.03	1.00	924	0.18	0.13	413	0.02	0.06	10.01	0.06		0.03	6.03	0.93	0.38	0.699
1.82	0.96	98.01	0.98	1811	0.19	0.11	553	0.04	0.14	10.17	0.08	0.02	0.06	5.87	1.01	0.29	0.698
1.50	1.09	97.19	0.88	1775	0.17	0.12	547	0.04	0.11	10.22	0.07	0.03	0.06	5.89	0.84	0.33	0.828
1.42	1.02	97.49	0.83	1685	0.17	0.12	533	0.04	0.15	10.11	0.07	0.04	0.06	5.93	0.80	0.31	0.897
1.26	1.37	97.05	0.84	1183	0.16	0.13	445	0.03	0.14	10.19	0.09	0.08	0.04	5.91	0.71	0.41	0.874
1.41	1.09	97.72	0.84	2645	0.16	0.12	665	0.06	0.07	10.21	0.08	0.03	0.09	5.87	0.79	0.33	0.887
2.64	0.92	98.78	1.32	1203	0.22	0.11	447	0.05	0.05	10.32	0.07	0.03	0.04	5.78	1.47	0.27	0.263
1.50	1.04	97.79	0.87	1463	0.17	0.12	490	0.06	0.12	10.23	0.08	0.02	0.05	5.88	0.84	0.31	0.848
1.17	1.19	97.23	0.76	2188	0.21	0.17	708	0.03	0.08	10.01	0.04	0.04	0.07	6.02	0.65	0.36	0.989
1.27	1.15	98.06	0.80	1390	0.22	0.16	565	0.02	0.12	9.89	0.05	0.03	0.05	6.08	0.70	0.34	0.956
1.04	1.36	98.22	0.74	1774	0.20	0.18	638	0.06	0.17	9.76	0.06	0.06	0.06	6.07	0.57	0.40	1.025
1.22	1.19	98.60	0.78	2868	0.21	0.17	811	0.07	0.14	9.91	0.06	0.04	0.09	5.97	0.67	0.35	0.975
1.12	1.15	97.92	0.73	2153	0.20	0.16	703	0.05	0.14	9.85	0.05	0.03	0.07	6.06	0.62	0.34	1.041
1.20	1.23	98.50	0.78	4053	0.21	0.17	963	0.12	0.14	9.85	0.05	0.03	0.13	5.91	0.66	0.36	0.975
1.59	1.05	99.58	0.91	1140	0.24	0.16	512	0.04	0.13	9.93	0.04	0.03	0.04	6.04	0.87	0.31	0.826
1.25	1.17	98.33	0.79	2880	0.22	0.16	812	0.06	0.12	9.86	0.04	0.01	0.09	6.02	0.69	0.34	0.966
1.40	1.12	96.85	0.84	2012	0.23	0.16	678	0.05	0.06	10.03	0.04	0.03	0.07	5.99	0.79	0.34	0.877
1.20	1.27	97.50	0.79	2473	0.15	0.13	676	0.04	0.10	10.15	0.06		0.08	5.93	0.67	0.38	0.951
1.17	1.24	95.58	0.77	1475	0.15	0.13	521	0.04	0.09	10.33	0.07		0.05	5.90	0.67	0.38	0.948
1.33	1.33	98.55	0.86	2975	0.16	0.14	742	0.05	0.11	9.94	0.06		0.10	5.98	0.73	0.39	0.879
1.20	1.26	98.79	0.79	1251	0.15	0.13	481	0.02	0.09	10.11	0.06		0.04	6.02	0.66	0.37	0.964
1.30	1.24	97.41	0.83	1704	0.16	0.13	561	0.04	0.09	10.02	0.05		0.06	6.02	0.73	0.37	0.902
1.33	1.14	98.27	0.82	2558	0.16	0.13	687	0.04	0.11	10.20	0.06		0.08	5.91	0.74	0.34	0.922
1.20	1.15	98.16	0.76	1856	0.15	0.13	586	0.04	0.09	10.01	0.05		0.06	6.03	0.66	0.34	0.998
1.19	1.31	98.74	0.80	1159	0.15	0.13	463	0.02	0.11	10.11	0.06		0.04	6.02	0.66	0.39	0.958
1.05	1.25	98.39	0.72	911	0.14	0.13	410	0.03	0.13	9.99	0.07		0.03	6.07	0.58	0.37	1.051
2.77	0.84	99.02	1.36	604	0.22	0.10	312	0.02	0.11	10.25	0.07	0.03	0.02	5.82	1.53	0.25	0.219
1.26	1.26	98.72	0.82	912	0.16	0.13	396	0.02	0.11	10.13	0.07	0.05	0.03	5.99	0.70	0.37	0.928
1.23	1.24	97.79	0.80	678	0.16	0.13	342	0.02	0.11	10.05	0.06	0.05	0.02	6.04	0.69	0.37	0.946
1.24	1.35	98.69	0.83	1567	0.16	0.13	519	0.04	0.13	10.10	0.06	0.06	0.05	5.95	0.69	0.40	0.913
2.10	0.97	98.71	1.10	1392	0.20	0.11	488	0.04	0.12	10.18	0.05	0.02	0.05	5.88	1.16	0.29	0.550
1.29	1.13	99.13	0.80	1514	0.16	0.12	509	0.04	0.11	10.03	0.06	0.03	0.05	6.01	0.71	0.33	0.961
1.29	1.14	97.91	0.80	1451	0.16	0.12	498	0.03	0.12	10.18	0.07	0.03	0.05	5.95	0.72	0.34	0.942
2.25	1.15	99.54	1.21	1637	0.20	0.12	513	0.06	0.11	9.98	0.06	0.03	0.05	5.91	1.23	0.34	0.432
2.39	1.02	98.83	1.24	882	0.21	0.12	387	0.02	0.08	10.18	0.07	0.03	0.03	5.88	1.32	0.30	0.375
1.14	1.26	97.61	0.76	1750	0.15	0.13	572	0.04	0.12	10.14	0.06	0.00	0.06	5.97	0.64	0.38	0.986
1.64	0.99	97.05	0.91	1346	0.18	0.11	473	0.03	0.11	10.30	0.06	0.03	0.05	5.88	0.92	0.30	0.776
1.50	*1.19*			*1656*													
0.46	*0.15*			*687*													
1.31	*1.18*			*1541*													

F	Cl	Total	O = F,Cl	S ppm	stdev F (wt%)	stdev Cl (wt%)	stdev S (ppm)	Si	Fe	Ca	Mg	Mn	S	P	F	Cl	OH*
2.08	0.83	98.11	1.06	1135	0.20	0.11	458	0.03	0.08	10.16	0.06		0.04	5.93	1.16	0.25	0.597
1.44	1.03	98.44	0.84	1875	0.16	0.12	589	0.04	0.10	10.08	0.06		0.06	5.97	0.79	0.31	0.899
2.52	1.40	99.88	1.38	1013	0.22	0.14	433	0.04	0.13	9.92	0.05		0.03	5.93	1.38	0.41	0.215
2.61	1.07	98.84	1.34	1383	0.22	0.12	506	0.03	0.10	10.05	0.05		0.05	5.89	1.44	0.32	0.247
2.14	0.98	97.28	1.12	813	0.20	0.12	387	0.02	0.09	10.36	0.07		0.03	5.85	1.20	0.30	0.498
2.44	1.01	99.21	1.26	2187	0.21	0.12	635	0.04	0.12	10.02	0.06		0.07	5.87	1.34	0.30	0.362
1.70	0.96	98.89	0.93	465	0.18	0.11	293	0.01	0.05	10.12	0.06		0.02	6.04	0.94	0.28	0.782
2.23	0.92	100.39	1.15	1269	0.20	0.11	484	0.05	0.10	9.97	0.07		0.04	5.96	1.21	0.27	0.527
2.46	0.92	93.38	1.24	1022	0.21	0.11	433	0.06	0.09	10.36	0.04		0.04	5.76	1.45	0.29	0.263
2.80	0.92	100.40	1.39	943	0.23	0.11	417	0.03	0.18	9.92	0.07		0.03	5.91	1.52	0.27	0.215
2.01	1.00	98.91	1.07	1733	0.19	0.12	566	0.03	0.10	10.10	0.06		0.06	5.93	1.11	0.29	0.599
2.32	0.78	99.61	1.15	1087	0.21	0.10	449	0.03	0.05	9.94	0.06		0.03	6.02	1.26	0.23	0.515
1.34	1.09	98.22	0.81	1934	0.16	0.12	598	0.04	0.11	10.05	0.05		0.06	6.00	0.74	0.32	0.938
2.79	1.33	98.58	1.47	1353	0.23	0.14	500	0.07	0.09	9.95	0.05		0.04	5.87	1.54	0.39	0.067
1.38	1.03	97.59	0.81	1797	0.16	0.12	576	0.05	0.12	9.97	0.06		0.06	6.02	0.77	0.31	0.928
2.62	0.93	100.25	1.31	1948	0.22	0.11	600	0.04	0.16	9.92	0.06		0.06	5.90	1.42	0.27	0.307

159	1121-67	Open to matrix	15 nA, 30s on peak	Rb	Brujo	Dome		0.28	0.72		0.21	53.89	40.05	0.56
161	1121-67	Open to matrix	15 nA, 30s on peak	Rb	Brujo	Dome		0.09	0.50		0.23	53.77	40.65	0.20
13	2002-69	Open to matrix	15 nA, 30s on peak	Re	Mitad	Dome		0.22	0.53		0.23	53.64	40.19	0.38
20	2002-69	Open to matrix	15 nA, 30s on peak	Re	Mitad	Dome		0.24	0.87		0.33	53.99	39.13	0.21
169	SG-09-38	Open to matrix	15 nA, 30s on peak	ReA	Mitad	Flow		0.45	0.68	0.20	0.31	53.74	39.22	0.35
194	SG-09-38	Open to matrix (rim)	15 nA, 30s on peak	ReA	Mitad	Flow		0.30	0.82	0.24	0.23	54.06	39.36	0.47
13	SG-09-30	Open to matrix	15 nA, 30s on peak	RbC	Brujo	Flow		0.19	0.68	0.23	0.24	54.61	39.93	0.19
14	SG-09-30	Open to matrix	15 nA, 30s on peak	RbC	Brujo	Flow		0.24	0.85	0.26	0.21	53.74	41.15	0.30
20	SG-09-30	Open to matrix	15 nA, 30s on peak	RbC	Brujo	Flow		0.19	0.48	0.18	0.24	54.77	38.98	0.26
32	SG-09-30	Open to matrix (rim)	15 nA, 30s on peak	RbC	Brujo	Flow		0.32	1.14	0.30	0.23	53.34	38.53	0.32
50	SG-09-30	Open to matrix (rim)	15 nA, 30s on peak	RbC	Brujo	Flow		0.48	0.69	0.21	0.24	54.18	38.35	0.90
53	SG-09-30	Open to matrix	15 nA, 30s on peak	RbC	Brujo	Flow		0.10	0.60	0.25	0.24	54.05	38.82	0.17
76	2003-69	Open to matrix	15 nA, 30s on peak	Re	Mitad	Dome		0.19	0.73	0.26	0.34	53.77	39.34	0.41
111	SG-09-01	Open to matrix	15 nA, 30s on peak	RcM1	Caliente	Flow		0.33	0.89	0.14	0.35	53.70	38.49	0.28
113	SG-09-01	Open to matrix	15 nA, 30s on peak	RcM1	Caliente	Flow		0.20	0.68	0.14	0.28	54.13	39.90	0.48
122	SG-09-01	Open to matrix	15 nA, 30s on peak	RcM1	Caliente	Flow		0.22	0.78	0.16	0.25	54.10	39.33	0.39
175	SG-09-07	Open to matrix (rim)	15 nA, 30s on peak	RcM3	Caliente	Flow		0.08	0.57	0.13	0.24	54.71	38.58	0.09
177	SG-09-07	Open to matrix	15 nA, 30s on peak	RcM3	Caliente	Flow		0.13	1.19	0.21	0.28	54.41	39.47	0.12
180	SG-09-07	Open to matrix	15 nA, 30s on peak	RcM3	Caliente	Flow		0.24	0.99	0.15	0.22	53.99	38.68	0.40
192	SG-09-04	Open to matrix	15 nA, 30s on peak	RcL	Caliente	Flow		0.20	0.64	0.19	0.28	54.06	38.96	0.38
212	SG-09-04	Open to matrix	15 nA, 30s on peak	RcL	Caliente	Flow		0.18	0.62	0.15	0.26	54.42	40.32	0.20
218	SG-09-04	Open to matrix	15 nA, 30s on peak	RcL	Caliente	Flow		0.12	0.55	0.14	0.27	53.67	39.09	0.42
220	SG-09-04	Open to matrix (rim)	15 nA, 30s on peak	RcL	Caliente	Flow		0.14	0.62	0.11	0.26	54.03	38.69	0.22
235	SG-09-04	Open to matrix	15 nA, 30s on peak	RcL	Caliente	Flow		0.21	0.64	0.17	0.29	53.53	40.31	0.44
244	802-66	Open to matrix	15 nA, 30s on peak	RmA	Monje	Flow		0.14	0.43	0.17	0.22	53.94	38.95	0.24
							Mean	*0.22*	*0.71*	*0.19*	*0.25*	*53.92*	*39.70*	*0.34*
							stdev	*0.09*	*0.21*	*0.05*	*0.04*	*0.47*	*0.98*	*0.15*
							Median	*0.21*	*0.68*	*0.18*	*0.24*	*53.99*	*39.91*	*0.33*

Point identifier	Sample number			Unit	Vent	Type		SiO_2	FeO	MnO	MgO	CaO	P_2O_5	SO_3
78	2006-69	Microphenocryst	15 nA, 30s on peak	-	Caliente	Bomb		0.13	0.47		0.23	53.98	40.44	0.27
152	1121-67	Microphenocryst	15 nA, 30s on peak	Rb	Brujo	Dome		0.09	0.61		0.23	53.70	40.83	0.18
153	1121-67	Microphenocryst	15 nA, 30s on peak	Rb	Brujo	Dome		0.15	0.62		0.21	53.85	40.26	0.26
158	1121-67	Microphenocryst	15 nA, 30s on peak	Rb	Brujo	Dome		0.15	0.46		0.22	54.25	41.04	0.33
3	2002-69	Microphenocryst	15 nA, 30s on peak	Re	Mitad	Dome		0.16	0.39		0.20	53.90	40.67	0.40
4	2002-69	Microphenocryst	15 nA, 30s on peak	Re	Mitad	Dome		0.43	0.69		0.21	53.42	39.15	0.34
9	2002-69	Microphenocryst	15 nA, 30s on peak	Re	Mitad	Dome		0.22	0.51		0.20	53.78	40.31	0.36
14	2002-69	Microphenocryst	15 nA, 30s on peak	Re	Mitad	Dome		0.36	0.45		0.20	53.44	39.80	0.05
22	2002-69	Microphenocryst	15 nA, 30s on peak	Re	Mitad	Dome		0.24	0.64		0.20	53.35	38.86	0.25
24	SG-09-36	Microphenocryst	15 nA, 30s on peak	ReA	Mitad	Flow		0.13	0.44	0.13	0.27	54.17	38.95	0.28
172	SG-09-38	Microphenocryst	15 nA, 30s on peak	ReA	Mitad	Flow		0.15	0.62	0.17	0.22	54.14	38.13	0.26
10	SG-09-30	Microphenocryst	15 nA, 30s on peak	RbC	Brujo	Flow		0.13	0.59	0.20	0.23	54.30	40.09	0.12
11	SG-09-30	Microphenocryst	15 nA, 30s on peak	RbC	Brujo	Flow		0.08	0.35	0.16	0.23	54.30	40.93	0.11
65	2003-69	Microphenocryst	15 nA, 30s on peak	Re	Mitad	Dome		0.11	0.27	0.21	0.21	54.88	39.16	0.21
128	SG-09-01	Microphenocryst	15 nA, 30s on peak	RcM1	Caliente	Flow		0.19	0.60	0.18	0.21	54.46	38.83	0.23
160	SG-09-07	Microphenocryst	15 nA, 30s on peak	RcM3	Caliente	Flow		0.19	0.35	0.08	0.22	54.54	39.78	0.42
161	SG-09-07	Microphenocryst	15 nA, 30s on peak	RcM3	Caliente	Flow		0.20	0.50	0.16	0.23	54.56	38.35	0.44
162	SG-09-07	Microphenocryst	15 nA, 30s on peak	RcM3	Caliente	Flow		0.25	0.57	0.12	0.24	54.15	38.46	0.48
163	SG-09-07	Microphenocryst	15 nA, 30s on peak	RcM3	Caliente	Flow		0.18	0.26	0.13	0.18	54.68	39.56	0.34
165	SG-09-07	Microphenocryst	15 nA, 30s on peak	RcM3	Caliente	Flow		0.10	0.38	0.12	0.27	54.80	39.93	0.19
166	SG-09-07	Microphenocryst	15 nA, 30s on peak	RcM3	Caliente	Flow		0.21	0.60	0.12	0.28	54.03	39.23	0.52
195	SG-09-04	Microphenocryst	15 nA, 30s on peak	RcL	Caliente	Flow		0.18	0.45	0.13	0.26	54.17	39.40	0.27
196	SG-09-04	Microphenocryst	15 nA, 30s on peak	RcL	Caliente	Flow		0.31	0.53	0.15	0.24	54.31	37.30	0.26
197	SG-09-04	Microphenocryst	15 nA, 30s on peak	RcL	Caliente	Flow		0.17	0.43	0.16	0.29	54.08	38.55	0.30
206	SG-09-04	Microphenocryst	15 nA, 30s on peak	RcL	Caliente	Flow		0.20	0.57	0.11	0.26	54.15	38.86	0.41
229	SG-09-04	Microphenocryst	15 nA, 30s on peak	RcL	Caliente	Flow		0.15	0.58	0.19	0.27	54.13	38.55	0.21
34172_a1_6	SG-09-05	Microphenocryst	10 nA, 120 s on peak	RcL	Caliente	Flow		0.17	0.76	0.11	0.18	53.11	41.32	0.61
34172_a3_1	SG-09-05	Microphenocryst	10 nA, 120 s on peak	RcL	Caliente	Flow		0.18	0.62	0.19	0.15	53.58	41.69	0.33
34183_ap1_1	SG-09-16	Microphenocryst (rim)	10 nA, 120 s on peak	-	Caliente	Lahar deposit		0.19	0.38	0.18	0.16	53.38	40.94	0.25
34183_ap1_2	SG-09-16	Microphenocryst (core)	10 nA, 120 s on peak	-	Caliente	Lahar deposit		0.19	0.37	0.20	0.16	52.98	39.00	0.32
34183_ap1_3	SG-09-16	Microphenocryst (rim)	10 nA, 120 s on peak	-	Caliente	Lahar deposit		0.24	0.36	0.12	0.18	53.08	40.34	0.50
34183_ap10_1	SG-09-16	Microphenocryst (rim)	10 nA, 120 s on peak	-	Caliente	Lahar deposit		0.20	0.33	0.20	0.19	53.44	41.00	0.47
34183_ap10_2	SG-09-16	Microphenocryst (rim)	10 nA, 120 s on peak	-	Caliente	Lahar deposit		0.41	0.64	0.19	0.16	53.15	40.50	0.72
34183_ap3_1	SG-09-16	Microphenocryst	10 nA, 120 s on peak	-	Caliente	Lahar deposit		0.40	0.36	0.13	0.16	53.10	39.42	0.99
34204_ap12_1	SG-09-38	Microphenocryst	10 nA, 120 s on peak	ReA	Mitad	Flow		0.09	0.42	0.18	0.16	54.11	42.23	0.35
34204_ap1_1	SG-09-38	Microphenocryst	10 nA, 120 s on peak	ReA	Mitad	Flow		0.04	0.40	0.11	0.14	52.99	41.55	0.20
34204_ap10_1	SG-09-38	Microphenocryst	10 nA, 120 s on peak	ReA	Mitad	Flow		0.17	0.55	0.19	0.14	53.54	41.18	0.40
34204_ap3_1	SG-09-38	Microphenocryst (rim)	10 nA, 120 s on peak	ReA	Mitad	Flow		0.07	0.25	0.09	0.15	53.75	41.73	0.20
34204_ap3_2	SG-09-38	Microphenocryst (rim)	10 nA, 120 s on peak	ReA	Mitad	Flow		0.06	0.72	0.12	0.14	53.83	40.87	0.12
34204_ap4_1	SG-09-38	Microphenocryst (core)	10 nA, 120 s on peak	ReA	Mitad	Flow		0.27	0.87	0.13	0.19	52.35	40.31	1.01
34204_ap4_2	SG-09-38	Microphenocryst (rim)	10 nA, 120 s on peak	ReA	Mitad	Flow		0.22	0.40	0.21	0.15	53.47	40.60	0.33
							Mean	*0.19*	*0.50*	*0.15*	*0.20*	*53.84*	*39.95*	*0.35*
							stdev	*0.09*	*0.14*	*0.04*	*0.04*	*0.56*	*1.14*	*0.20*
							Median	*0.18*	*0.47*	*0.16*	*0.21*	*53.90*	*40.09*	*0.32*

1.88	1.00	99.22	1.02	1912	0.19	0.12	594	0.04	0.10	9.99	0.07		0.06	5.97	1.03	0.29	0.681
2.18	0.96	98.85	1.13	2232	0.20	0.11	642	0.05	0.11	10.04	0.05		0.07	5.90	1.20	0.28	0.519
1.20	1.08	97.70	0.75	786	0.15	0.12	381	0.02	0.07	10.13	0.06		0.03	6.05	0.66	0.32	1.013
2.65	1.20	99.04	1.39	1518	0.22	0.13	533	0.04	0.08	9.97	0.06		0.05	5.90	1.46	0.35	0.191
2.20	1.40	98.37	1.24	825	0.20	0.14	392	0.04	0.13	10.20	0.09		0.03	5.84	1.23	0.42	0.354
2.49	1.01	98.45	1.28	1411	0.21	0.11	476	0.08	0.10	10.10	0.08	0.03	0.05	5.82	1.38	0.30	0.318
2.79	0.97	99.25	1.39	1890	0.22	0.11	550	0.05	0.12	10.08	0.06	0.04	0.06	5.80	1.54	0.28	0.177
3.10	0.69	99.85	1.46	754	0.24	0.10	360	0.03	0.10	10.11	0.06	0.03	0.02	5.84	1.70	0.20	0.104
3.17	0.89	100.81	1.53	1206	0.25	0.11	455	0.04	0.12	9.80	0.05	0.04	0.04	5.93	1.70	0.26	0.039
3.01	0.64	98.76	1.41	1054	0.24	0.09	425	0.03	0.07	10.28	0.06	0.03	0.03	5.78	1.67	0.19	0.139
2.95	1.03	98.16	1.48	1297	0.24	0.12	471	0.06	0.17	10.10	0.06	0.04	0.04	5.76	1.65	0.31	0.041
2.77	0.89	98.72	1.37	3602	0.23	0.11	784	0.08	0.10	10.17	0.06	0.03	0.12	5.69	1.54	0.26	0.200
2.66	1.50	98.39	1.46	678	0.23	0.14	340	0.02	0.09	10.23	0.06	0.04	0.02	5.81	1.48	0.45	0.067
2.58	1.33	98.94	1.39	1641	0.22	0.13	527	0.03	0.11	10.07	0.09	0.04	0.05	5.82	1.43	0.39	0.178
2.43	0.89	97.48	1.22	1109	0.22	0.11	432	0.06	0.13	10.23	0.09	0.02	0.04	5.79	1.36	0.27	0.368
1.69	0.99	98.49	0.93	1938	0.18	0.11	572	0.04	0.10	10.15	0.07	0.02	0.06	5.91	0.94	0.29	0.772
2.04	0.93	98.19	1.07	1556	0.20	0.11	512	0.04	0.11	10.21	0.06	0.02	0.05	5.86	1.14	0.28	0.584
2.74	0.74	97.89	1.32	375	0.23	0.10	249	0.01	0.08	10.40	0.06	0.02	0.01	5.79	1.54	0.22	0.240
2.13	0.81	98.75	1.08	475	0.20	0.10	281	0.02	0.18	10.24	0.07	0.03	0.02	5.87	1.19	0.24	0.574
2.31	0.99	97.98	1.20	1594	0.21	0.11	514	0.04	0.15	10.24	0.06	0.02	0.05	5.80	1.29	0.30	0.408
1.58	1.03	97.33	0.90	1517	0.17	0.12	501	0.04	0.10	10.31	0.07	0.03	0.05	5.87	0.89	0.31	0.800
2.80	1.15	100.12	1.44	809	0.23	0.12	365	0.03	0.09	10.05	0.07	0.02	0.03	5.88	1.53	0.34	0.138
1.58	1.10	96.95	0.91	1695	0.17	0.12	528	0.02	0.08	10.25	0.07	0.02	0.06	5.90	0.89	0.33	0.776
1.79	0.98	96.84	0.97	866	0.18	0.11	377	0.03	0.09	10.36	0.07	0.02	0.03	5.87	1.01	0.30	0.691
1.55	1.05	98.19	0.89	1747	0.17	0.12	536	0.04	0.09	10.04	0.08	0.02	0.06	5.97	0.86	0.31	0.830
1.25	1.11	96.44	0.78	958	0.15	0.12	396	0.02	0.06	10.38	0.06	0.03	0.03	5.92	0.71	0.34	0.953
2.25	*1.01*			*1367*													
0.54	*0.18*			*602*													
2.31	*0.99*			*1325*													

F	Cl	Total	O = F,Cl	S ppm	stdev F (wt%)	stdev Cl (wt%)	stdev S (ppm)	Si	Fe	Ca	Mg	Mn	S	P	F	Cl	OH*
2.21	0.98	98.71	1.15	1097	0.20	0.12	450	0.02	0.07	10.07	0.06		0.04	5.96	1.22	0.29	0.496
2.67	1.02	99.35	1.36	733	0.22	0.12	368	0.02	0.09	9.94	0.06		0.02	5.97	1.46	0.30	0.241
2.34	0.86	98.56	1.18	1061	0.21	0.11	442	0.03	0.09	10.06	0.06		0.03	5.94	1.29	0.25	0.453
2.75	0.81	100.01	1.34	1306	0.23	0.11	491	0.03	0.07	9.96	0.06		0.04	5.95	1.49	0.23	0.275
1.83	1.05	98.60	1.01	1616	0.19	0.12	550	0.03	0.06	10.05	0.05		0.05	5.99	1.01	0.31	0.686
1.70	0.96	96.88	0.93	1352	0.18	0.12	503	0.08	0.10	10.19	0.06		0.05	5.90	0.96	0.29	0.756
1.85	1.00	98.23	1.01	1447	0.19	0.12	520	0.04	0.07	10.08	0.05		0.05	5.97	1.02	0.30	0.678
1.57	1.10	96.95	0.91	207	0.17	0.12	197	0.06	0.07	10.17	0.05		0.01	5.98	0.88	0.33	0.788
1.67	1.16	96.38	0.96	1010	0.18	0.13	434	0.04	0.10	10.26	0.05		0.03	5.90	0.95	0.35	0.700
2.46	0.91	97.73	1.24	1133	0.22	0.11	434	0.02	0.06	10.27	0.07	0.02	0.04	5.84	1.37	0.27	0.353
2.68	0.86	97.23	1.32	1037	0.22	0.10	408	0.03	0.09	10.36	0.06	0.03	0.03	5.77	1.52	0.26	0.224
2.39	0.81	98.87	1.19	500	0.22	0.10	293	0.02	0.09	10.15	0.06	0.03	0.02	5.92	1.32	0.24	0.441
2.81	1.16	100.13	1.44	447	0.23	0.12	277	0.01	0.05	9.99	0.06	0.02	0.01	5.95	1.52	0.34	0.138
2.35	1.07	98.47	1.23	850	0.21	0.12	380	0.02	0.04	10.35	0.06	0.03	0.03	5.84	1.31	0.32	0.375
2.89	0.70	98.30	1.38	926	0.23	0.10	394	0.03	0.09	10.28	0.06	0.03	0.03	5.79	1.61	0.21	0.180
2.54	1.06	99.18	1.31	1662	0.22	0.12	526	0.03	0.05	10.16	0.06	0.01	0.05	5.85	1.40	0.31	0.289
2.36	0.78	97.58	1.17	1768	0.21	0.10	542	0.04	0.07	10.39	0.06	0.02	0.06	5.77	1.33	0.23	0.440
2.09	1.01	97.37	1.11	1920	0.20	0.11	565	0.04	0.09	10.33	0.06	0.02	0.06	5.79	1.18	0.31	0.517
2.19	1.15	98.65	1.18	1345	0.20	0.12	473	0.03	0.04	10.26	0.05	0.02	0.04	5.87	1.21	0.34	0.447
1.81	1.01	98.61	0.99	747	0.19	0.11	352	0.02	0.06	10.29	0.07	0.02	0.02	5.92	1.01	0.30	0.694
1.86	1.01	97.86	1.01	2072	0.19	0.11	587	0.04	0.09	10.22	0.07	0.02	0.07	5.86	1.04	0.30	0.662
1.69	1.00	97.55	0.94	1085	0.18	0.11	423	0.03	0.07	10.28	0.07	0.02	0.04	5.91	0.95	0.30	0.753
2.64	0.91	96.64	1.32	1059	0.22	0.11	417	0.06	0.08	10.49	0.07	0.02	0.04	5.69	1.50	0.28	0.217
1.81	0.98	96.77	0.98	1217	0.18	0.11	448	0.03	0.06	10.38	0.08	0.02	0.04	5.84	1.02	0.30	0.679
1.78	1.07	97.42	0.99	1630	0.18	0.12	518	0.04	0.09	10.31	0.07	0.02	0.05	5.85	1.00	0.32	0.678
1.71	0.94	96.74	0.93	843	0.18	0.11	372	0.03	0.09	10.41	0.07	0.03	0.03	5.86	0.97	0.29	0.741
1.42	1.16	98.83	0.86	2452	0.23	0.16	750	0.03	0.11	9.84	0.05	0.02	0.08	6.05	0.78	0.34	0.885
1.46	1.09	99.30	0.86	1335	0.23	0.16	553	0.03	0.09	9.89	0.04	0.03	0.04	6.08	0.80	0.32	0.885
2.03	0.85	98.33	1.04	981	0.28	0.14	475	0.03	0.05	9.95	0.04	0.03	0.03	6.03	1.12	0.25	0.634
1.57	1.03	95.82	0.89	1264	0.24	0.15	537	0.03	0.06	10.22	0.04	0.03	0.04	5.94	0.90	0.31	0.791
1.55	1.01	97.37	0.88	2004	0.24	0.15	676	0.04	0.05	10.00	0.05	0.02	0.07	6.01	0.86	0.30	0.838
1.38	1.06	98.27	0.82	1873	0.23	0.16	654	0.04	0.05	9.97	0.05	0.03	0.06	6.05	0.76	0.31	0.928
1.71	1.02	98.50	0.95	2884	0.25	0.15	811	0.07	0.09	9.90	0.04	0.03	0.09	5.96	0.94	0.30	0.762
1.61	1.08	97.24	0.92	3947	0.24	0.16	947	0.07	0.05	10.03	0.04	0.02	0.13	5.88	0.90	0.32	0.780
1.36	1.04	99.93	0.81	1392	0.23	0.16	566	0.02	0.06	9.91	0.04	0.03	0.04	6.11	0.74	0.30	0.963
1.34	1.08	97.85	0.81	793	0.22	0.16	426	0.01	0.06	9.91	0.04	0.02	0.03	6.14	0.74	0.32	0.939
2.06	1.06	99.30	1.11	1613	0.28	0.16	606	0.03	0.08	9.89	0.04	0.03	0.05	6.01	1.12	0.31	0.566
1.92	1.08	99.23	1.05	808	0.27	0.16	430	0.01	0.04	9.92	0.04	0.01	0.03	6.08	1.04	0.32	0.639
1.92	1.09	98.87	1.05	476	0.27	0.16	330	0.01	0.10	10.03	0.04	0.02	0.02	6.02	1.06	0.32	0.623
1.38	1.17	97.68	0.85	4039	0.23	0.16	959	0.05	0.13	9.82	0.05	0.02	0.13	5.97	0.76	0.35	0.889
1.99	0.83	98.19	1.03	1316	0.27	0.14	548	0.04	0.06	10.00	0.04	0.03	0.04	6.00	1.10	0.25	0.654
1.98	*1.00*			*1396*													
0.45	*0.11*			*804*													
1.86	*1.02*			*1264*													

Santiaguito apatites are similar to those of some other subduction-related systems for which data are available (Fig. 3). Apatite sulphur contents are similar in all textural associations. Those fully included in their host phenocrysts contain on average 1656 ppm S (1 σ 687 ppm; n = 52), while those that are open to the matrix contain 1367 ppm S (1 σ 602 ppm, n = 42) and microphenocrysts contain 1396 ppm S (1 σ 804 ppm; n = 41; Table 1). In other words, the mean S concentrations from the population of apatites in each textural category are separated by less than one standard deviation. However, the data suggest that there are detectable differences in halogen concentrations for apatite in different textural situations (Table 1; see also Supplementary Figure), with the mean values of each apatite category separated by more than 1 standard deviation. Microphenocrysts record higher mean fluorine contents (1.98 wt% F, 1 σ 0.45 wt%) and lower mean chlorine (1.00 wt% Cl, 1 σ 0.11 wt%) than inclusions within phenocrysts (1.50 wt% F, 1 σ 0.46 wt% and 1.19 wt% Cl, 1 σ 0.15 wt%). Median concentrations are slightly lower for the microphenocrysts and inclusions (Table 1), reflecting a spread of a minority of data points to high F contents. Inclusions that are partially open to the matrix tend to record slightly higher mean F (2.25 wt%, 1 σ 0.54 wt%) but similar mean Cl (1.01 wt%, 1 σ 0.18 wt%) to the microphenocrysts. The rims of individual microphenocrysts systematically record lower Cl and higher F than the cores. We estimated OH contents for apatite using stoichiometry and assuming a fully occupied Z site (e.g. Piccoli and Candela, 2002); average calculated OH contents are 0.82 pfu for the apatite inclusions, compared with 0.46 pfu for inclusions open to the matrix and 0.60 pfu for the microphenocrysts (see Table 1). However, propagated OH uncertainties are very high and the assumption of complete stoichiometry may be unrealistic, particularly if significant C is present (e.g. Suetsugu et al., 2000).

Element mapping of individual crystals confirms that S, F, and Cl zoning is common even in very small apatites, but demonstrates that the form of the zoning may be quite variable. Apatites containing melt inclusions, or those entrapped adjacent to melt inclusions in the host phenocryst, commonly have patches enriched in F and Cl adjacent to the melt; S contents tend to be unaffected (Fig. 4a). Included apatites may contain sulphur-rich cores but typically do not show significant zoning of halogens. Inclusions open to the matrix also typically contain sulphur-rich cores and may show enrichment in fluorine towards the matrix, but with no equivalent systematic pattern in Cl contents (Fig. 4). Microphenocrysts may have sulphur-rich cores, and typically show F-rich rims (Fig. 4). Some grains show more complex sulphur zoning (Fig. 4).

4.2. Matrix glass compositions

The glass analyses presented include matrix glass, glass embayments at the margins of phenocrysts and glass trapped within glomerocrysts. The supplementary data from Scott et al. (2013) are given together with the new data in Table 2. Matrix glasses show a continuous range from 66–80 wt% SiO_2 and follow systematic major element variations. All the glasses show decreasing CaO, Na_2O and Al_2O_3 and increasing K_2O with increasing SiO_2. The MgO, CaO, FeO and TiO_2 contents of the matrix glasses decrease systematically with increasing bulk rock SiO_2 content, and the least evolved matrix glasses become more Si-rich (Fig. 5). The glasses plot along a systematic trend in the haplogranite ternary, and this has been interpreted as reflecting decompression crystallisation (Scott et al., 2012, fig. 11).

Glasses from most individual samples show a clear increase of K_2O and TiO_2 with increasing SiO_2, with glasses from the most evolved bulk rocks falling to lower concentrations at >75 wt% SiO_2, but the overall picture is scattered (Fig. 5). A similar overall pattern is seen for FeO although the degree of scatter is higher and the downturn to lower FeO contents occurs at lower SiO_2. FeO does not correlate with K_2O or Al_2O_3, but correlates well with MgO (Fig. 5). The matrix glass compositions generally compare well with those of plagioclase-hosted melt inclusions from the 1902 dacite pumice and basaltic andesite scoria (Singer et al., 2014; Fig. 5). The glomerocryst interstitial glasses are similar to the matrix glass, but with slightly lower CaO, slightly higher K_2O and TiO_2, and markedly higher FeO (Fig. 5).

Analytical totals are high in all the glasses analysed (Table 2), which suggests low dissolved H_2O concentrations. The matrix glasses contain up to 2400 ppm Cl, but the majority have much lower concentrations (average 835 ppm, 1 σ 352 ppm, Table 2; Fig. 6). Overall, variations of Cl with SiO_2 show a similar pattern to TiO_2, with concentrations increasing with fractionation and then dropping towards lower Cl contents in the most evolved glasses (Fig. 6). F concentrations were consistently below detection limits (~0.35 wt% F). Only a few glasses had sulphur contents above detection limit (~135 ppm S); these contained 0.05–0.13 wt% SO_3 (200–520 ppm S). The interstitial glasses from the glomerocrysts typically contain higher Cl concentrations (1780 ± 440 ppm Cl, Fig. 6) but similar sulphur concentrations to the matrix glasses.

These data are more or less consistent with previously reported glass compositions in samples erupted from Santa María–Santiaguito, with the exception of apparently low H_2O contents in our samples, inferred from the lack of significantly low analytical totals. Villemant et al. (2003) reported bulk groundmass compositions for dome rocks with 0.07–0.93 wt% H_2O and 114–676 ppm Cl, whereas the bulk groundmass of Plinian fall deposits contained typically 1–1.5 wt% H_2O and 780–950 ppm Cl. Volatile contents of matrix glass in clasts from the 1902 Plinian eruption were 0.55–2.4 wt% H_2O (estimated by difference) and 937–1397 ppm Cl (Villemant et al., 2003). Balcone-Boissard et al. (2010) reported similar halogen contents, also for melt inclusions from Plinian clasts from the 1902–1929 eruptions (100–300 ppm F, 700–1600 ppm Cl), but with much higher H_2O contents (estimated at 5–7 wt% H_2O). Singer et al. (2014) analysed H_2O in plagioclase-hosted melt inclusions from the 1902 dacite pumice by secondary ion mass spectrometry and recorded concentrations up to 6.85 wt% H_2O.

5. Discussion

5.1. Interpretation of glass compositional variations

Taken together, the matrix glass compositions exhibit chemical trends that indicate progressive fractionation driven by decompression and degassing; this is consistent with the progressive decrease in H_2O content seen in plagioclase-hosted melt inclusions (Singer et al., 2014). The increase in MgO, FeO, TiO_2 and K_2O with SiO_2 in individual samples suggests that fractionation is dominated by plagioclase ± pyroxene, consistent with the observed modal abundance of ~75–80% plagioclase within the phenocryst assemblage (Scott et al., 2013). The most silica-rich glasses can only have formed at very low pressures, and the wide range of normative SiO_2 contents seen in the whole dataset is consistent with crystallisation of hydrous magma over a wide pressure range (Blundy and Cashman, 2001). The presence of amphibole phenocrysts in some of the more evolved rocks indicates crystallisation at ~150 MPa or more (assuming H_2O saturation; e.g. Browne and Gardner, 2006). Phase equilibria experiments (Andrews, 2014) suggest that the Santa Maria 1902 dacite was stored at pressures similar to 150–170 MPa (if H_2O-saturated) at 850 °C prior to eruption. Face-value application of the thermobarometer proposed by Ridolfi et al. (2010) indicates crystallisation depths >12 km (Scott et al., 2013), and there is also geochemical evidence of substantial fractionation of amphibole from the magma, seen as a decrease in Dy/Yb with increasing SiO_2 and La/Lu in the whole-rock dataset of Scott et al. (2013). Although pressures predicted by the Ridolfi et al. (2010) barometer are likely to be over-estimated (Andrews, 2014; Erdmann et al., 2014), these data together indicate polybaric crystallisation in the Santa Maria – Santiaguito system. The interpretation of decompression crystallisation is supported by the well-developed groundmass and amphibole breakdown textures (Scott et al., 2012); the high H_2O contents of melt inclusions (Singer et al., 2014) and successful phase equilibria

Table 2
Electron microprobe analyses of glasses.

Point identifier	Sample number	Vent	Bulk rock SiO_2 wt%	SiO_2	TiO_2	Al_2O_3	FeO	MnO	MgO	CaO	Na_2O	K_2O	P_2O_5	SO_3	Cl	Total	stdev Cl wt%	S ppm	Cl ppm		Reference
1	SG-09-01	Caliente	61.99	76.23	0.62	10.76	2.87		0.98	0.95	3.51	3.86	0.31	bd	0.142	100.24	0.074		1424	Matrix glass	Scott et al. (2013) supplementary data
2	SG-09-01	Caliente	61.99	69.87	0.42	17.48	1.29		0.23	3.35	5.76	2.10	0.05	bd	0.046	100.59	0.042		455	Matrix glass	Scott et al. (2013) supplementary data
3	SG-09-01	Caliente	61.99	67.74	0.23	18.06	1.76		0.63	3.89	5.93	1.67	0.09	bd	0.046	100.04	0.042		464	Matrix glass	Scott et al. (2013) supplementary data
5	SG-09-01	Caliente	61.99	73.04	0.47	13.00	2.14		0.78	1.59	4.80	2.97	0.16	bd	0.063	99.02	0.049		629	Matrix glass	Scott et al. (2013) supplementary data
6	SG-09-01	Caliente	61.99	72.59	0.45	15.44	1.03		0.08	2.24	5.46	2.60	0.06	bd	0.051	100.00	0.045		514	Matrix glass	Scott et al. (2013) supplementary data
7	SG-09-01	Caliente	61.99	70.53	0.43	16.46	1.14		0.24	3.00	5.41	2.42	0.12	bd	0.062	99.81	0.049		619	Matrix glass	Scott et al. (2013) supplementary data
10	SG-09-01	Caliente	61.99	67.38	0.41	17.82	2.03		0.43	3.54	5.98	1.62	0.09	bd	bd	99.30				Matrix glass	Scott et al. (2013) supplementary data
11	SG-09-01	Caliente	61.99	69.54	0.44	16.68	2.18		0.44	3.53	5.32	2.34	0.20	bd	bd	100.67				Matrix glass	Scott et al. (2013) supplementary data
13	SG-09-01	Caliente	61.99	74.00	0.40	14.06	1.51		0.29	1.84	4.92	2.95	0.18	bd	0.047	m	0.042		465	Matrix glass	Scott et al. (2013) supplementary data
14	SG-09-01	Caliente	61.99	71.46	0.35	16.27	0.96		0.11	2.60	5.85	1.98	0.04	bd	0.060	99.69	0.048		601	Matrix glass	Scott et al. (2013) supplementary data
15	SG-09-01	Caliente	61.99	74.87	0.60	12.09	2.68		0.76	1.29	4.39	3.32	0.20	bd	0.069	100.27	0.052		687	Matrix glass	Scott et al. (2013) supplementary data
16	SG-09-01	Caliente	61.99	75.17	0.66	12.30	2.44		0.49	1.05	4.49	3.39	0.13	bd	0.085	100.22	0.057		852	Matrix glass	Scott et al. (2013) supplementary data
17	SG-09-01	Caliente	61.99	71.26	0.44	15.34	1.99		0.39	2.42	5.13	2.62	0.16	bd	0.062	99.82	0.049		618	Matrix glass	Scott et al. (2013) supplementary data
18	SG-09-01	Caliente	61.99	77.91	0.57	11.58	1.38		0.18	0.43	4.05	3.92	0.08	bd	0.094	100.19	0.060		941	Matrix glass	Scott et al. (2013) supplementary data
19	SG-09-07	Caliente	62.38	70.75	0.44	14.37	1.94		0.45	2.24	5.14	3.38	0.31	bd	0.078	99.09	0.055		781	Matrix glass	Scott et al. (2013) supplementary data
21	SG-09-07	Caliente	62.38	68.87	0.57	16.70	2.23		0.09	3.52	6.15	1.47	0.09	bd	bd	99.69				Matrix glass	Scott et al. (2013) supplementary data
23	SG-09-07	Caliente	62.38	75.34	0.44	13.04	1.28		0.12	0.91	4.42	4.46	0.09	bd	0.141	100.25	0.074		1411	Matrix glass	Scott et al. (2013) supplementary data
25	SG-09-07	Caliente	62.38	68.86	0.36	16.39	2.00		0.54	3.46	5.18	2.87	0.32	bd	0.076	100.04	0.054		761	Matrix glass	Scott et al. (2013) supplementary data
26	SG-09-07	Caliente	62.38	74.82	0.60	11.47	2.25		0.56	0.94	3.81	4.36	0.17	bd	0.132	99.11	0.071		1316	Matrix glass	Scott et al. (2013) supplementary data
27	SG-09-07	Caliente	62.38	71.73	0.35	15.73	1.35		0.38	2.81	5.36	2.46	0.28	bd	0.047	100.49	0.043		474	Matrix glass	Scott et al. (2013) supplementary data
51	SG-09-05	Caliente	62.52	68.53	0.30	17.99	1.37		0.25	3.65	6.01	1.99	0.15	bd	bd	100.25				Matrix glass	Scott et al. (2013) supplementary data
52	SG-09-05	Caliente	62.52	72.37	0.44	14.96	1.76		0.30	2.10	5.72	2.54	0.08	bd	0.067	100.34	0.051		673	Matrix glass	Scott et al. (2013) supplementary data
53	SG-09-05	Caliente	62.52	76.78	0.69	11.49	2.22		0.35	0.65	4.19	3.61	0.13	bd	0.103	100.21	0.063		1030	Matrix glass	Scott et al. (2013) supplementary data
54	SG-09-05	Caliente	62.52	76.43	0.63	12.11	2.18		0.31	0.86	4.48	3.59	0.10	bd	0.096	100.79	0.061		962	Matrix glass	Scott et al. (2013) supplementary data
58	SG-09-05	Caliente	62.52	70.59	0.42	15.85	1.90		0.61	3.01	5.15	2.49	0.17	bd	0.041	100.25	0.040		412	Matrix glass	Scott et al. (2013) supplementary data
59	SG-09-05	Caliente	62.52	75.50	0.57	11.77	2.34		0.61	0.98	4.21	3.45	0.26	bd	0.078	99.77	0.055		779	Matrix glass	Scott et al. (2013) supplementary data
60	SG-09-05	Caliente	62.52	70.44	0.45	16.62	1.62		0.23	3.14	5.59	2.37	0.10	bd	0.067	100.63	0.051		671	Matrix glass	Scott et al. (2013) supplementary data
61	SG-09-05	Caliente	62.52	76.18	0.62	12.63	1.80		0.08	0.86	4.70	3.36	0.10	bd	0.084	100.42	0.057		836	Matrix glass	Scott et al. (2013) supplementary data
62	SG-09-05	Caliente	62.52	76.28	0.61	12.33	1.47		0.08	0.72	4.67	3.54	0.13	bd	0.078	99.90	0.055		780	Matrix glass	Scott et al. (2013) supplementary data
63	SG-09-05	Caliente	62.52	72.24	0.44	15.80	1.32		0.12	2.50	5.73	2.56	0.11	bd	0.052	100.85	0.045		518	Matrix glass	Scott et al. (2013) supplementary data
64	SG-09-05	Caliente	62.52	71.64	0.47	15.27	1.59		0.27	2.58	5.55	2.59	0.19	bd	0.052	100.19	0.045		518	Matrix glass	Scott et al. (2013) supplementary data
66	SG-09-05	Caliente	62.52	75.05	0.59	12.86	1.56		0.07	1.11	4.56	3.43	0.07	bd	0.088	99.39	0.058		875	Matrix glass	Scott et al. (2013) supplementary data
67	SG-09-05	Caliente	62.52	72.67	0.41	15.04	1.45		0.06	2.05	5.40	2.68	0.05	bd	0.075	99.88	0.054		749	Matrix glass	Scott et al. (2013) supplementary data
69	SG-09-05	Caliente	62.52	67.46	0.30	18.40	1.21		0.09	4.19	5.87	1.85	0.10	bd	0.050	99.51	0.044		496	Matrix glass	Scott et al. (2013) supplementary data
70	SG-09-04	Caliente	62.56	71.62	0.33	16.35	1.22		0.08	2.63	5.76	2.32	0.11	bd	0.060	100.49	0.048		604	Matrix glass	Scott et al. (2013) supplementary data
71	SG-09-04	Caliente	62.56	76.34	0.52	12.66	1.86		0.31	1.03	4.47	3.18	0.11	bd	0.073	100.54	0.053		731	Matrix glass	Scott et al. (2013) supplementary data
72	SG-09-04	Caliente	62.56	73.82	0.52	13.57	1.60		0.25	1.51	4.87	3.07	0.20	bd	0.087	99.49	0.058		873	Matrix glass	Scott et al. (2013) supplementary data
73	SG-09-04	Caliente	62.56	77.71	0.59	11.88	1.79		0.04	0.50	4.30	3.78	0.06	bd	0.108	100.75	0.064		1075	Matrix glass	Scott et al. (2013) supplementary data
75	SG-09-04	Caliente	62.56	77.69	0.58	11.81	1.76		0.13	0.55	4.27	3.77	0.14	0.076	0.092	100.87	0.060	304	922	Matrix glass	Scott et al. (2013) supplementary data
76	SG-09-04	Caliente	62.56	68.82	0.31	17.85	1.27		0.13	3.63	5.93	2.05	0.07	bd	0.041	100.10	0.040		411	Matrix glass	Scott et al. (2013) supplementary data
77	SG-09-04	Caliente	62.56	67.44	0.34	18.45	1.41		0.26	4.25	5.78	1.68	0.26	bd	0.067	99.94	0.051		670	Matrix glass	Scott et al. (2013) supplementary data
78	SG-09-04	Caliente	62.56	69.85	0.38	16.98	1.33		0.25	3.01	6.01	2.12	0.07	bd	bd	100.01				Matrix glass	Scott et al. (2013) supplementary data
79	SG-09-04	Caliente	62.56	76.12	0.53	12.69	1.48		0.07	0.89	4.63	3.58	0.10	bd	bd	100.09				Matrix glass	Scott et al. (2013) supplementary data
80	SG-09-04	Caliente	62.56	70.18	0.32	16.99	1.43		0.18	3.12	5.90	2.08	0.11	bd	bd	100.30				Matrix glass	Scott et al. (2013) supplementary data
81	SG-09-04	Caliente	62.56	76.52	0.54	12.64	1.57		0.04	0.78	4.63	3.54	0.10	bd	0.084	100.45	0.057		837	Matrix glass	Scott et al. (2013) supplementary data
82	SG-09-04	Caliente	62.56	75.28	0.58	13.15	1.51		0.06	1.28	4.51	3.41	0.15	bd	0.086	100.01	0.057		856	Matrix glass	Scott et al. (2013) supplementary data
83	SG-09-04	Caliente	62.56	77.69	0.56	12.10	1.59		0.08	0.54	4.38	3.69	0.10	bd	0.081	100.82	0.056		808	Matrix glass	Scott et al. (2013) supplementary data
84	SG-09-04	Caliente	62.56	77.99	0.60	11.91	1.39		0.06	0.43	4.31	3.77	0.13	bd	0.071	100.67	0.052		711	Matrix glass	Scott et al. (2013) supplementary data
88	SG-09-03	Caliente	62.41	72.02	0.50	15.07	1.37		0.16	2.24	5.16	2.81	0.13	bd	0.063	99.51	0.049		631	Matrix glass	Scott et al. (2013) supplementary data
89	SG-09-03	Caliente	62.41	74.39	0.66	11.86	2.76		0.69	0.95	4.04	3.59	0.17	bd	0.077	99.18	0.054		773	Matrix glass	Scott et al. (2013) supplementary data
90	SG-09-03	Caliente	62.41	70.90	0.47	15.97	0.92		0.12	2.74	5.40	2.64	0.09	bd	0.057	99.31	0.047		573	Matrix glass	Scott et al. (2013) supplementary data
91	SG-09-03	Caliente	62.41	72.73	0.44	13.90	2.05		0.62	1.88	5.41	1.88	0.12	bd	bd	99.02				Matrix glass	Scott et al. (2013) supplementary data
92	SG-09-03	Caliente	62.41	74.84	0.62	12.18	1.74		0.36	0.95	4.18	3.75	0.21	bd	0.129	98.96	0.070		1290	Matrix glass	Scott et al. (2013) supplementary data
93	SG-09-03	Caliente	62.41	66.08	0.27	18.09	2.25		1.01	4.19	5.76	1.64	0.22	bd	0.040	99.53	0.039		400	Matrix glass	Scott et al. (2013) supplementary data

(continued on next page)

Table 2 (*continued*)

Point identifier	Sample number	Vent	Bulk rock SiO_2 wt%	SiO_2	TiO_2	Al_2O_3	FeO	MnO	MgO	CaO	Na_2O	K_2O	P_2O_5	SO_3	Cl	Total	stdev Cl wt%	S ppm	Cl ppm		Reference
94	SG-09-03	Caliente	62.41	67.27	0.30	18.67	1.24		0.28	3.79	6.07	1.71	0.12	bd	bd	99.45				Matrix glass	Scott et al. (2013) supplementary data
95	SG-09-03	Caliente	62.41	76.57	0.64	11.15	1.73		0.19	0.39	3.77	4.21	0.11	bd	0.160	98.92	0.078		1597	Matrix glass	Scott et al. (2013) supplementary data
97	SG-09-03	Caliente	62.41	75.18	0.51	13.76	0.90		0.06	1.26	4.88	3.43	0.10	bd	0.054	100.13	0.045		536	Matrix glass	Scott et al. (2013) supplementary data
98	SG-09-03	Caliente	62.41	71.69	0.44	15.85	1.17		0.17	2.51	5.10	2.87	0.08	bd	0.082	99.96	0.056		820	Matrix glass	Scott et al. (2013) supplementary data
99	SG-09-03	Caliente	62.41	77.08	0.57	12.05	1.10		0.11	0.62	4.33	4.01	0.11	bd	0.075	100.06	0.053		746	Matrix glass	Scott et al. (2013) supplementary data
100	SG-09-03	Caliente	62.41	76.96	0.66	11.48	2.10		0.22	0.61	3.83	4.07	0.27	bd	0.085	100.29	0.057		849	Matrix glass	Scott et al. (2013) supplementary data
102	SG-09-03	Caliente	62.41	71.37	0.42	16.08	1.19		0.12	2.64	5.41	2.59	0.05	bd	0.087	99.95	0.057		867	Matrix glass	Scott et al. (2013) supplementary data
103	SG-09-03	Caliente	62.41	68.67	0.42	16.96	2.12		0.44	4.04	5.04	2.30	0.10	bd	0.062	100.16	0.048		617	Matrix glass	Scott et al. (2013) supplementary data
2	SG-09-09	Lahar	62.76	74.05	0.70	11.50	3.16		0.74	0.94	4.25	3.66	0.20	bd	0.160	99.38	0.076		1595	Matrix glass	Scott et al. (2013) supplementary data
7	SG-09-09	Lahar	62.76	74.56	0.70	11.98	2.43		0.22	0.52	4.39	4.40	0.05	0.078	0.239	99.57	0.087	314	2393	Matrix glass	Scott et al. (2013) supplementary data
8	SG-09-09	Lahar	62.76	73.54	0.66	12.38	2.42		0.28	0.93	5.69	2.57	0.08	bd	0.159	98.69	0.071		1589	Matrix glass	Scott et al. (2013) supplementary data
11	1234-67	-	-	67.89	0.21	17.83	1.15		0.25	3.51	5.67	1.98	0.06	bd	0.064	98.61	0.045		644	Matrix glass	Scott et al. (2013) supplementary data
12	1234-67	-	-	78.16	0.41	11.68	1.12		0.18	0.68	4.13	3.57	0.11	bd	0.116	100.15	0.061		1160	Matrix glass	Scott et al. (2013) supplementary data
13	1234-67	-	-	73.89	0.23	15.15	1.18		0.31	2.03	5.41	2.39	0.14	bd	0.070	100.80	0.047		701	Matrix glass	Scott et al. (2013) supplementary data
14	1234-67	-	-	68.84	0.19	18.61	1.14		0.28	3.36	6.74	1.56	0.06	bd	bd	100.77				Matrix glass	Scott et al. (2013) supplementary data
15	1234-67	-	-	72.69	0.27	14.77	1.26		0.36	1.78	5.20	2.57	0.05	bd	0.069	99.01	0.048		686	Matrix glass	Scott et al. (2013) supplementary data
16	1234-67	-	-	75.75	0.40	13.39	1.47		0.13	1.36	4.60	3.09	0.13	bd	0.068	100.39	0.051		681	Matrix glass	Scott et al. (2013) supplementary data
35	SG-09-06	Caliente	63.08	68.84	0.25	18.17	1.47		0.29	3.73	6.13	1.74	0.07	bd	bd	100.69				Matrix glass	Scott et al. (2013) supplementary data
37	SG-09-06	Caliente	63.08	77.43	0.55	11.38	1.51		0.23	0.60	4.06	4.16	0.19	bd	0.106	100.21	0.064		1062	Matrix glass	Scott et al. (2013) supplementary data
38	SG-09-06	Caliente	63.08	76.81	0.45	12.26	1.62		0.35	0.92	4.26	3.70	0.14	bd	0.073	100.57	0.053		734	Matrix glass	Scott et al. (2013) supplementary data
39	SG-09-06	Caliente	63.08	73.74	0.42	13.98	1.67		0.39	2.23	4.79	3.18	0.15	bd	0.077	100.62	0.055		771	Matrix glass	Scott et al. (2013) supplementary data
40	SG-09-06	Caliente	63.08	76.69	0.50	12.08	1.72		0.14	0.77	4.29	3.69	0.16	bd	0.100	100.15	0.062		1003	Matrix glass	Scott et al. (2013) supplementary data
41	SG-09-06	Caliente	63.08	68.24	0.29	17.61	1.21		0.34	3.91	5.81	1.87	0.11	bd	bd	99.38				Matrix glass	Scott et al. (2013) supplementary data
42	SG-09-06	Caliente	63.08	72.20	0.35	14.67	2.14		0.58	2.32	5.36	2.71	0.20	bd	0.076	100.60	0.054		760	Matrix glass	Scott et al. (2013) supplementary data
44	SG-09-06	Caliente	63.08	74.24	0.42	14.05	1.03		0.18	1.60	4.96	2.91	0.07	bd	0.067	99.52	0.051		666	Matrix glass	Scott et al. (2013) supplementary data
45	SG-09-06	Caliente	63.08	70.21	0.37	16.31	1.81		0.63	3.01	5.46	2.37	0.16	bd	0.089	100.42	0.058		885	Matrix glass	Scott et al. (2013) supplementary data
49	SG-09-06	Caliente	63.08	67.98	0.29	18.35	1.50		0.31	3.80	6.07	1.82	0.15	bd	0.058	100.33	0.047		577	Matrix glass	Scott et al. (2013) supplementary data
18	SG-09-38	Mitad	63.28	75.15	0.33	13.65	1.52		0.08	1.35	5.09	3.12	0.02	bd	0.062	100.35	0.049		622	Matrix glass	Scott et al. (2013) supplementary data
19	SG-09-38	Mitad	63.28	67.40	0.29	17.90	1.21		0.03	3.21	6.23	2.11	0.06	bd	0.028	98.48	0.033		281	Matrix glass	Scott et al. (2013) supplementary data
21	SG-09-38	Mitad	63.28	74.94	0.37	14.10	1.30		0.22	1.70	5.01	2.86	0.12	bd	0.079	100.71	0.055		788	Matrix glass	Scott et al. (2013) supplementary data
22	SG-09-38	Mitad	63.28	72.26	0.38	15.24	1.49		0.23	2.56	5.04	2.62	0.25	bd	0.076	100.13	0.054		757	Matrix glass	Scott et al. (2013) supplementary data
23	SG-09-38	Mitad	63.28	74.73	0.41	13.55	1.70		0.32	1.45	4.60	3.05	0.08	bd	0.088	99.97	0.058		875	Matrix glass	Scott et al. (2013) supplementary data
24	SG-09-23	Caliente	64.91	70.93	0.18	16.62	1.09		0.32	2.15	6.11	2.59	0.09	bd	0.029	100.09	0.034		291	Matrix glass	Scott et al. (2013) supplementary data
29	SG-09-29	Brujo	63.78	72.40	0.28	15.67	1.03		0.05	2.15	4.73	3.44	0.07	bd	0.072	99.88	0.053		717	Matrix glass	Scott et al. (2013) supplementary data
33	SG-09-29	Brujo	63.78	76.44	0.40	12.14	0.83		0.04	0.53	4.44	3.25	0.09	bd	0.090	98.25	0.059		896	Matrix glass	Scott et al. (2013) supplementary data
1	SG-09-32	Monje	64.1	78.57	0.15	12.47	0.27		0.00	1.37	4.67	2.13	0.05	bd	bd	99.68				Matrix glass	Scott et al. (2013) supplementary data
2	SG-09-32	Monje	64.1	79.99	0.33	10.77	0.89		0.25	0.33	3.51	3.41	0.04	bd	0.044	99.55	0.042		441	Matrix glass	Scott et al. (2013) supplementary data
4	SG-09-32	Monje	64.1	77.44	0.21	11.67	0.58		0.09	0.87	4.09	3.05	0.08	bd	0.049	98.13	0.044		488	Matrix glass	Scott et al. (2013) supplementary data
5	SG-09-32	Monje	64.1	73.19	0.50	14.07	1.34		0.23	0.41	3.75	5.12	0.04	bd	0.197	98.85	0.087		1974	Matrix glass	Scott et al. (2013) supplementary data
6	SG-09-32	Monje	64.1	76.71	0.37	12.46	0.93		0.03	0.62	4.01	3.91	0.02	bd	0.097	99.15	0.061		971	Matrix glass	Scott et al. (2013) supplementary data
8	SG-09-32	Monje	64.1	73.40	0.26	15.21	1.05		0.23	2.09	5.45	2.56	0.03	bd	0.091	100.36	0.059		912	Matrix glass	Scott et al. (2013) supplementary data
9	SG-09-32	Monje	64.1	70.79	0.12	16.88	0.60		0.01	2.53	6.13	2.51	0.02	bd	bd	99.62				Matrix glass	Scott et al. (2013) supplementary data

13	SG-09-32	Monje	64.1	77.45	0.17	12.93	0.36	0.00	0.66	4.88	3.56	0.03	bd	bd	100.04				Matrix glass	Scott et al. (2013) supplementary data
14	SG-09-32	Monje	64.1	79.57	0.38	10.71	1.25	0.07	0.54	3.66	2.79	0.06	bd	bd	99.03				Matrix glass	Scott et al. (2013) supplementary data
16	SG-09-32	Monje	64.1	73.70	0.14	14.47	0.69	0.09	1.58	5.47	2.76	0.08	bd	0.054	99.05	0.046		543	Matrix glass	Scott et al. (2013) supplementary data
17	SG-09-32	Monje	64.1	77.98	0.20	12.10	0.41	0.00	0.85	4.68	3.03	0.04	bd	bd	99.30				Matrix glass	Scott et al. (2013) supplementary data
18	SG-09-34	Monje	64.59	75.50	0.71	11.36	2.91	0.40	0.57	3.54	4.69	0.11	bd	0.174	99.97	0.082		1744	Matrix glass	Scott et al. (2013) supplementary data
19	SG-09-34	Monje	64.59	70.99	0.28	17.00	0.90	0.11	2.45	6.03	2.39	0.07	bd	0.067	100.29	0.051		667	Matrix glass	Scott et al. (2013) supplementary data
20	SG-09-34	Monje	64.59	75.73	0.32	13.76	1.06	0.12	1.28	4.75	3.31	0.10	bd	0.100	100.54	0.062		998	Matrix glass	Scott et al. (2013) supplementary data
22	SG-09-34	Monje	64.59	70.52	0.27	16.72	1.13	0.17	2.69	5.39	2.96	0.08	bd	0.083	100.01	0.057		829	Matrix glass	Scott et al. (2013) supplementary data
23	SG-09-34	Monje	64.59	74.85	0.30	13.57	1.84	0.55	1.42	5.06	2.80	0.05	bd	0.074	100.52	0.054		744	Matrix glass	Scott et al. (2013) supplementary data
24	SG-09-34	Monje	64.59	69.96	0.23	17.41	1.07	0.17	2.81	6.15	2.39	0.07	0.082	0.069	100.41	0.052	327	694	Matrix glass	Scott et al. (2013) supplementary data
25	SG-09-34	Monje	64.59	76.33	0.43	11.81	1.63	0.49	0.87	4.17	4.00	0.19	bd	0.104	100.02	0.063		1042	Matrix glass	Scott et al. (2013) supplementary data
26	SG-09-34	Monje	64.59	76.09	0.23	13.35	0.67	0.17	1.64	5.08	2.07	0.12	bd	0.040	99.46	0.039		398	Matrix glass	Scott et al. (2013) supplementary data
28	SG-09-34	Monje	64.59	77.46	0.48	10.66	1.58	0.12	0.20	3.44	4.92	0.09	bd	0.107	99.06	0.064		1071	Matrix glass	Scott et al. (2013) supplementary data
31	SG-09-34	Monje	64.59	76.79	0.38	12.48	1.12	0.33	1.44	4.17	2.68	0.33	bd	0.100	99.81	0.062		998	Matrix glass	Scott et al. (2013) supplementary data
32	SG-09-34	Monje	64.59	70.03	0.25	16.98	0.78	0.16	2.53	6.05	1.75	0.08	bd	bd	98.60				Matrix glass	Scott et al. (2013) supplementary data
33	SG-09-34	Monje	64.59	75.86	0.19	14.07	0.63	0.06	1.96	5.26	1.74	0.05	bd	bd	99.83				Matrix glass	Scott et al. (2013) supplementary data
34	SG-09-34	Monje	64.59	72.29	0.42	14.28	1.94	0.51	1.73	4.46	3.80	0.18	bd	0.071	99.67	0.052		714	Matrix glass	Scott et al. (2013) supplementary data
35	2006-69	Caliente	-	78.41	0.39	11.87	1.27	0.15	0.84	4.38	3.06	0.05	bd	0.076	100.49	0.054		757	Matrix glass	Scott et al. (2013) supplementary data
36	2006-69	Caliente	-	68.63	0.24	18.19	0.99	0.15	3.76	5.87	1.92	0.05	bd	bd	99.79				Matrix glass	Scott et al. (2013) supplementary data
37	2006-69	Caliente	-	73.38	0.22	14.25	1.51	0.55	1.63	5.73	2.37	0.04	bd	0.048	99.74	0.043		484	Matrix glass	Scott et al. (2013) supplementary data
38	2006-69	Caliente	-	68.13	0.21	19.42	0.86	0.05	4.03	6.07	1.89	0.06	bd	0.042	100.75	0.040		424	Matrix glass	Scott et al. (2013) supplementary data
39	2006-69	Caliente	-	76.76	0.47	11.19	1.96	0.29	0.60	3.70	3.99	0.27	bd	0.117	99.34	0.067		1169	Matrix glass	Scott et al. (2013) supplementary data
41	2006-69	Caliente	-	77.00	0.42	12.76	1.04	0.07	1.13	4.52	3.05	0.06	bd	0.088	100.14	0.058		880	Matrix glass	Scott et al. (2013) supplementary data
42	2006-69	Caliente	-	74.56	0.36	13.57	1.48	0.08	1.29	4.51	3.57	0.07	bd	0.084	99.57	0.057		837	Matrix glass	Scott et al. (2013) supplementary data
43	2006-69	Caliente	-	70.99	0.29	16.34	1.33	0.07	2.40	5.75	2.57	0.09	bd	0.044	99.88	0.041		442	Matrix glass	Scott et al. (2013) supplementary data
45	2006-69	Caliente	-	75.01	0.35	12.90	1.28	0.08	0.99	4.66	3.32	0.07	bd	0.106	98.77	0.064		1060	Matrix glass	Scott et al. (2013) supplementary data
46	2006-69	Caliente	-	74.91	0.38	13.57	1.07	0.07	1.36	5.19	2.80	0.05	bd	0.050	99.45	0.044		501	Matrix glass	Scott et al. (2013) supplementary data
47	2006-69	Caliente	-	69.82	0.19	17.39	1.11	0.23	3.44	5.74	1.62	0.11	bd	bd	99.65				Matrix glass	Scott et al. (2013) supplementary data
48	2006-69	Caliente	-	78.91	0.41	10.71	1.57	0.07	0.35	3.70	3.77	0.05	bd	bd	99.54				Matrix glass	Scott et al. (2013) supplementary data
49	2006-69	Caliente	-	77.73	0.44	11.70	1.32	0.10	0.61	4.44	3.40	0.07	bd	0.088	99.90	0.058		877	Matrix glass	Scott et al. (2013) supplementary data
51	SG-09-24	Caliente	65.92	73.79	0.12	13.70	0.93	0.34	1.39	4.87	2.89	0.07	bd	0.056	98.18	0.046		558	Matrix glass	Scott et al. (2013) supplementary data
53	SG-09-24	Caliente	65.92	77.12	0.31	11.08	1.76	0.68	0.91	3.82	3.07	0.16	0.082	0.136	99.13	0.072	327	1358	Matrix glass	Scott et al. (2013) supplementary data
54	SG-09-24	Caliente	65.92	77.91	0.21	12.30	0.63	0.16	1.04	4.46	2.79	0.00	bd	0.054	99.54	0.046		541	Matrix glass	Scott et al. (2013) supplementary data
55	SG-09-24	Caliente	65.92	75.95	0.31	12.28	0.99	0.16	0.77	4.07	3.57	0.05	bd	0.115	98.27	0.066		1146	Matrix glass	Scott et al. (2013) supplementary data
56	SG-09-24	Caliente	65.92	76.86	0.16	13.31	0.54	0.19	1.56	5.11	2.18	0.05	bd	bd	99.96				Matrix glass	Scott et al. (2013) supplementary data
57	SG-09-24	Caliente	65.92	75.97	0.18	13.34	0.76	0.28	1.54	5.09	2.40	0.11	bd	bd	99.67				Matrix glass	Scott et al. (2013) supplementary data
58	SG-09-24	Caliente	65.92	79.65	0.25	11.27	0.58	0.11	1.00	4.44	2.05	0.07	bd	bd	99.42				Matrix glass	Scott et al. (2013) supplementary data
59	SG-09-24	Caliente	65.92	79.18	0.16	11.51	0.69	0.09	0.78	3.95	2.87	0.08	bd	0.050	99.35	0.044		502	Matrix glass	Scott et al. (2013) supplementary data
60	SG-09-24	Caliente	65.92	75.56	0.21	13.04	0.71	0.15	1.15	4.68	2.99	0.08	bd	0.065	98.64	0.050		645	Matrix glass	Scott et al. (2013) supplementary data
61	SG-09-24	Caliente	65.92	78.46	0.16	12.25	0.60	0.21	1.04	4.73	2.84	0.08	bd	bd	100.39				Matrix glass	Scott et al. (2013) supplementary data
62	SG-09-24	Caliente	65.92	74.90	0.31	14.25	0.81	0.33	1.66	5.10	2.47	0.11	bd	bd	99.93				Matrix glass	Scott et al. (2013) supplementary data
63	SG-09-24	Caliente	65.92	76.59	0.38	12.62	1.14	0.16	1.24	4.36	3.40	0.07	bd	0.135	100.09	0.072		1345	Matrix glass	Scott et al. (2013) supplementary data
66	SG-09-24	Caliente	65.92	75.15	0.16	13.98	0.50	0.18	1.51	5.11	2.69	0.06	bd	bd	99.34				Matrix glass	Scott et al. (2013) supplementary data
67	SG-09-24	Caliente	65.92	74.48	0.25	13.19	1.45	0.41	0.94	4.43	3.90	0.02	bd	0.117	99.16	0.067		1168	Matrix glass	Scott et al. (2013) supplementary data
69	1000-67	Mitad	65.74	67.17	0.49	17.95	1.25	0.07	3.39	5.34	3.06	0.12	bd	0.164	99.00	0.079		1638	Matrix glass	Scott et al. (2013) supplementary data

(continued on next page)

Table 2 (*continued*)

Point identifier	Sample number	Vent	Bulk rock SiO_2 wt%	SiO_2	TiO_2	Al_2O_3	FeO	MnO	MgO	CaO	Na_2O	K_2O	P_2O_5	SO_3	Cl	Total	stdev Cl wt%	S ppm	Cl ppm		Reference
74	1000-67	Mitad	65.74	68.45	0.47	17.55	1.35		0.06	3.53	5.28	2.76	0.14	bd	0.114	99.71	0.066		1144	Matrix glass	Scott et al. (2013) supplementary data
83	1000-67	Mitad	65.74	66.57	0.46	18.61	1.15		0.08	4.01	5.64	2.58	0.14	bd	0.018	99.26	0.026		181	Matrix glass	Scott et al. (2013) supplementary data
84	1000-67	Mitad	65.74	69.65	0.58	16.58	1.50		0.04	2.44	5.47	3.62	0.21	bd	0.143	100.23	0.074		1427	Matrix glass	Scott et al. (2013) supplementary data
85	1121-67	Brujo	-	75.69	0.61	11.50	2.48		0.36	0.62	4.23	3.83	0.17	bd	0.087	99.57	0.058		870	Matrix glass	Scott et al. (2013) supplementary data
86	1121-67	Brujo	-	74.16	0.38	14.32	1.25		0.15	1.44	5.15	3.37	0.12	bd	0.088	100.43	0.058		879	Matrix glass	Scott et al. (2013) supplementary data
88	1121-67	Brujo	-	75.35	0.31	12.34	1.88		0.82	1.21	4.51	2.87	0.25	bd	0.086	99.62	0.057		860	Matrix glass	Scott et al. (2013) supplementary data
89	1121-67	Brujo	-	77.83	0.35	11.20	1.09		0.05	0.66	3.85	3.33	0.06	bd	0.075	98.50	0.053		747	Matrix glass	Scott et al. (2013) supplementary data
90	1121-67	Brujo	-	74.02	0.34	13.41	1.47		0.34	1.12	4.87	3.36	0.12	bd	0.071	99.13	0.052		707	Matrix glass	Scott et al. (2013) supplementary data
92	1121-67	Brujo	-	68.90	0.22	18.22	0.77		0.09	2.63	6.84	2.31	0.05	bd	0.049	100.09	0.043		486	Matrix glass	Scott et al. (2013) supplementary data
93	1121-67	Brujo	-	70.93	0.29	15.25	1.75		0.47	2.09	4.97	3.33	0.11	0.089	0.082	99.37	0.056	358	819	Matrix glass	Scott et al. (2013) supplementary data
94	1121-67	Brujo	-	75.06	0.38	12.06	1.92		0.36	0.77	3.92	4.43	0.25	bd	0.156	99.31	0.077		1563	Matrix glass	Scott et al. (2013) supplementary data
95	1121-67	Brujo	-	77.06	0.49	11.44	1.58		0.21	0.30	3.76	4.62	0.03	bd	0.120	99.60	0.068		1202	Matrix glass	Scott et al. (2013) supplementary data
97	1121-67	Brujo	-	78.14	0.40	11.63	1.31		0.09	0.71	4.11	3.41	0.07	bd	0.072	99.95	0.052		718	Matrix glass	Scott et al. (2013) supplementary data
98	1121-67	Brujo	-	73.18	0.35	14.61	0.98		0.05	1.41	5.23	3.60	0.01	bd	0.094	99.52	0.060		943	Matrix glass	Scott et al. (2013) supplementary data
99	1121-67	Brujo	-	78.99	0.29	10.87	0.91		0.13	0.83	4.02	2.60	0.07	bd	0.070	98.79	0.052		700	Matrix glass	Scott et al. (2013) supplementary data
100	1121-67	Brujo	-	72.85	0.34	14.74	1.30		0.14	1.65	4.84	3.24	0.06	bd	0.121	99.28	0.068		1210	Matrix glass	Scott et al. (2013) supplementary data
34172_m5_1	SG-09-05	Caliente	63.08	73.59	0.51	14.66	1.53	0.05	0.09	1.65	5.27	3.08	0.15	bd	bd	100.60				Matrix glass	New data (this study)
34172_m7_2	SG-09-05	Caliente	63.08	74.47	0.60	13.53	2.16	0.01	0.16	0.77	4.66	3.88	0.16	bd	0.129	100.53	0.076		1285	Glomerocryst glass	New data (this study)
34172_m4_2	SG-09-05	Caliente	63.08	74.71	0.67	12.91	2.45	0.08	0.21	0.80	4.64	3.87	0.20	bd	0.226	100.75	0.101		2257	Glomerocryst glass	New data (this study)
34172_m7_1	SG-09-05	Caliente	63.08	74.20	0.72	13.29	2.52	0.07	0.16	0.80	4.87	3.76	0.19	bd	0.147	100.73	0.081		1465	Glomerocryst glass	New data (this study)
34172_m6_1	SG-09-05	Caliente	63.08	73.62	0.71	13.45	2.62	0.05	0.14	0.74	4.79	3.82	0.21	bd	0.222	100.37	0.100		2222	Glomerocryst glass	New data (this study)
34172_mg3_3	SG-09-05	Caliente	63.08	73.22	0.58	13.30	2.72	0.13	0.21	1.17	6.23	2.05	0.18	bd	0.170	99.98	0.088		1703	Glomerocryst glass	New data (this study)
34172_m6_3	SG-09-05	Caliente	63.08	75.03	0.71	12.16	2.75	0.16	0.37	0.84	4.32	3.59	0.20	bd	0.120	100.24	0.074		1203	Glomerocryst glass	New data (this study)
34172_mg4_1	SG-09-05	Caliente	63.08	71.87	0.61	14.80	2.89	0.16	0.20	1.45	6.41	1.95	0.19	bd	0.169	100.69	0.088		1693	Glomerocryst glass	New data (this study)
34172_m6_2	SG-09-05	Caliente	63.08	73.21	0.73	13.22	3.01	0.04	0.19	0.97	4.69	3.79	0.22	bd	0.244	100.32	0.105		2439	Glomerocryst glass	New data (this study)
34172_mg1_1	SG-09-05	Caliente	63.08	72.34	0.62	13.69	3.22	0.10	0.26	1.46	6.96	1.04	0.23	bd	0.219	100.14	0.100		2188	Glomerocryst glass	New data (this study)
34172_m3_4	SG-09-05	Caliente	63.08	73.69	0.82	11.12	4.29	0.18	0.83	1.59	4.24	3.33	0.28	0.068	0.180	100.61	0.090	274	1800	Glomerocryst glass	New data (this study)
34172_m3_3	SG-09-05	Caliente	63.08	71.02	0.82	12.30	4.52	0.03	0.78	2.17	4.57	3.66	0.26	bd	0.187	100.32	0.092		1866	Glomerocryst glass	New data (this study)
34183_mg1_3	SG-09-16	Caliente	-	69.42	0.39	17.20	1.79	0.07	0.33	3.53	5.37	2.13	0.14	bd	bd	100.37				Glomerocryst glass	New data (this study)
34183_mg1_2	SG-09-16	Caliente	-	75.96	0.62	12.25	2.17	0.05	0.11	0.67	4.58	3.92	0.11	bd	0.106	100.54	0.069		1059	Glomerocryst glass	New data (this study)
34183_mg4_1	SG-09-16	Caliente	-	72.40	0.58	14.11	2.51	0.08	0.20	0.91	5.39	3.84	0.18	bd	0.146	100.33	0.081		1463	Glomerocryst glass	New data (this study)
34183_mg3_2	SG-09-16	Caliente	-	73.54	0.64	12.63	2.57	0.05	0.21	0.95	4.68	3.50	0.19	bd	0.149	99.13	0.082		1488	Glomerocryst glass	New data (this study)
34183_mg4_2	SG-09-16	Caliente	-	71.94	0.63	13.77	3.05	0.16	0.34	1.12	5.02	3.63	0.21	0.048	0.192	100.12	0.093	191	1921	Glomerocryst glass	New data (this study)
34183_mg4_3	SG-09-16	Caliente	-	71.36	0.63	13.67	3.62	0.16	0.43	1.13	5.04	3.70	0.19	bd	0.244	100.18	0.105		2438	Glomerocryst glass	New data (this study)

experiments (Andrews, 2014); and positive correlations between FeO, TiO_2 and MgO, and CaO and Al_2O_3 in the glasses, suggesting crystallisation of pyroxene, Fe-Ti oxides and plagioclase.

The high FeO and TiO_2 contents of the glomerocryst glass embayments may support the interpretation that some of the erupted crystal load is derived from disaggregated plutonic material that represents the fractionation products of the magma, perhaps prior to saturation of Fe-Ti oxides. The glomerocryst and matrix glasses have very low H_2O contents compared with melt inclusion compositions reported in previous studies (c.f. Balcone-Boissard et al., 2010). We interpret this as variable diffusional loss of H_2O during magma ascent, degassing and crystallisation. However, the glomerocryst glasses retain high Cl and F concentrations, probably due to much slower (minimal) diffusion of halogens from these crystal clots during ascent. Overall, the glomerocryst glass compositions suggest that they represent partially re-equilibrated fragments of early-formed crystal mush.

5.2. Behaviour of the halogens

With SiO_2 or K_2O as an index of differentiation, Cl contents of the glasses increase during fractionation from ~0.03 wt% to >0.15 wt% Cl, then decrease after ~75 wt% SiO_2. This indicates incompatible behaviour of Cl until the later stages of crystallisation, when it undergoes exsolution into a fluid phase, consistent with the conclusions of Villemant et al. (2003) based on correlation between H_2O and Cl contents of glass. Fluorine concentrations of the glasses were below detection limits. However, we can use the volatile contents of apatite to give more information on the evolution of volatiles during magma ascent and crystallisation.

The F/Cl ratio of apatite is dependent on the ratio of halogen fugacities, f_{HF}/f_{HCl}, as well as temperature and pressure (Piccoli and Candela, 1994). Therefore, in the absence of additional information, the cause of the observed compositional change is difficult to determine without ambiguity. The observation of higher F and lower Cl contents in the apatite microphenocrysts relative to inclusions could be produced by decreasing temperature, or by increasing pressure (Doherty et al., 2014; Piccoli and Candela, 2002). Recent work also indicates that Cl partitioning between apatite and melt in the presence of a fluid phase is dependent primarily on melt halogen (Cl) concentration, with a subsidiary dependence on pressure (Cl concentrations in apatite increasing with decreasing pressure; Doherty et al., 2014; Webster et al., 2009). We cannot rule out that decreasing temperature during crystallisation played a role in the changing apatite compositions. However, a number of factors suggest that the changing apatite chemistry is related to compositional variations in the coexisting melt and/or fluid. Firstly, the correlation between H_2O and Cl in glasses (Villemant et al., 2003), indicates that the magma reached fluid saturation and exsolution resulted in decreasing Cl concentrations in the melt. Loss of Cl from the melt by exsolution of a fluid phase, together with incompatible, non-volatile behaviour of F (i.e. F does not migrate into the free fluid phase but increases in concentration in the melt) would be consistent with increasing f_{HF}/f_{HCl} during crystallisation and degassing. This would require loss of Cl to occur between crystallisation of the pyroxene or plagioclase phenocrysts (that host the apatite inclusions) and crystallisation of the apatite microphenocrysts.

The Cl depletion of microphenocryst rims relative to microphenocryst cores could also reflect primary variations in melt composition during apatite crystallisation, or re-equilibration of the microphenocrysts with the partially degassed matrix melt. The variability in halogen contents of apatites open to the matrix, and the small-scale zoning observed when inclusions are trapped adjacent to glass, indicates relatively rapid halogen diffusion in apatite. However, Cl zoning in the microphenocrysts is typically more diffuse than that seen in the partially enclosed crystals, and occurs on similar scales in all crystallographic orientations, whereas halogen diffusivities are strongly anisotropic (Brenan, 1994). This suggests that the microphenocrysts do in fact record primary growth zoning and not partial re-equilibration.

5.3. Behaviour of sulphur

The population of apatite analyses records a wide spread of sulphur concentrations and there is no statistically significant difference in S content between microphenocrysts and inclusions. However, the X-ray mapping shows that apatite microphenocryst cores are enriched in sulphur relative to the rims, with minor but detectable fluctuations between core and rim in some grains (see Fig. 4). Although early-formed sulphide inclusions are occasionally found in the cores of magnetite and pyroxene phenocrysts, no sulphides are found in the groundmass and this is consistent with the relatively high measured oxygen fugacity of $+1 < \Delta NNO < +2$ (Andrews, 2014; Singer et al., 2014). This suggests that sulphur is not compatible in any late-crystallising phase in these magmas, and therefore that the decrease in sulphur contents in apatite rims must indicate either a decrease in sulphur concentration in the melt resulting from degassing, or a decrease in the partition coefficient $D_S^{ap\text{-}m}$ due to a change in conditions in the magma. The S partition coefficient for apatite depends on oxygen fugacity (Peng et al., 1997), melt sulphur content and temperature (Parat and Holtz, 2004, 2005). At Santiaguito, we have no evidence for strong changes in magma oxygen fugacity, which is relatively high (estimates range from NNO + 0.5 to NNO + 2, Andrews, 2014; Scott et al., 2012; Singer et al., 2014). Temperature variations may have been important during magma fractionation and ascent, given that temperature estimates for the dacites are 860–885 °C but 925–1040 °C for the basaltic andesite (Singer et al., 2014). However, $D_S^{ap\text{-}m}$ increases with decreasing temperature (Parat and Holtz, 2004, see later), so cooling during fractionation would have the effect of increasing the S content of apatite in equilibrium with the melt, resulting in reverse zoning instead of the observed normal zoning. We therefore conclude that for the most part, the volatile contents of apatite at Santiaguito are related to changes in melt volatile concentration and degassing.

5.4. Quantification of pre-eruptive volatile contents

We used published apatite-melt partition coefficients to estimate pre-eruptive melt volatile concentrations from the analysed apatite compositions. Apatite inclusions in the phenocryst phases are essentially protected from the external melt environment and should therefore retain a reliable record of their original volatile contents, as long as they are not in contact with any melt pockets (see above; Fig. 4). To determine the volatile concentrations in the melt prior to ascent and degassing, we take representative compositions of apatite inclusions and the cores of microphenocrysts (Table 3). Volatile concentrations in the melt after decompression and immediately prior to extrusion are derived from matrix glass compositions.

5.4.1. Sulphur

We estimated $D_S^{ap\text{-}m}$ by first calculating the apatite saturation temperature (i.e., the temperature at which apatite appears on the liquidus), following Piccoli and Candela (1994) and Dietterich and De Silva (2010):

$$AST(K) = \frac{\left(26400 \cdot C_{SiO_2}^{AST} - 4800\right)}{12.4 \cdot C_{SiO_2}^{AST} - \ln\left(\frac{C_{P_2O_5}^{AST}}{1 - \frac{X}{100}}\right) - 3.97} \quad (1)$$

where AST is the apatite saturation temperature; $C^{AST}{}_{SiO2}$ and $C^{AST}{}_{P2O5}$ are the weight fractions of SiO_2 and P_2O_5 in the melt at the point of apatite saturation, and X is the fractional crystallinity of the magma at the point of apatite saturation. In the Santiaguito magmas there are

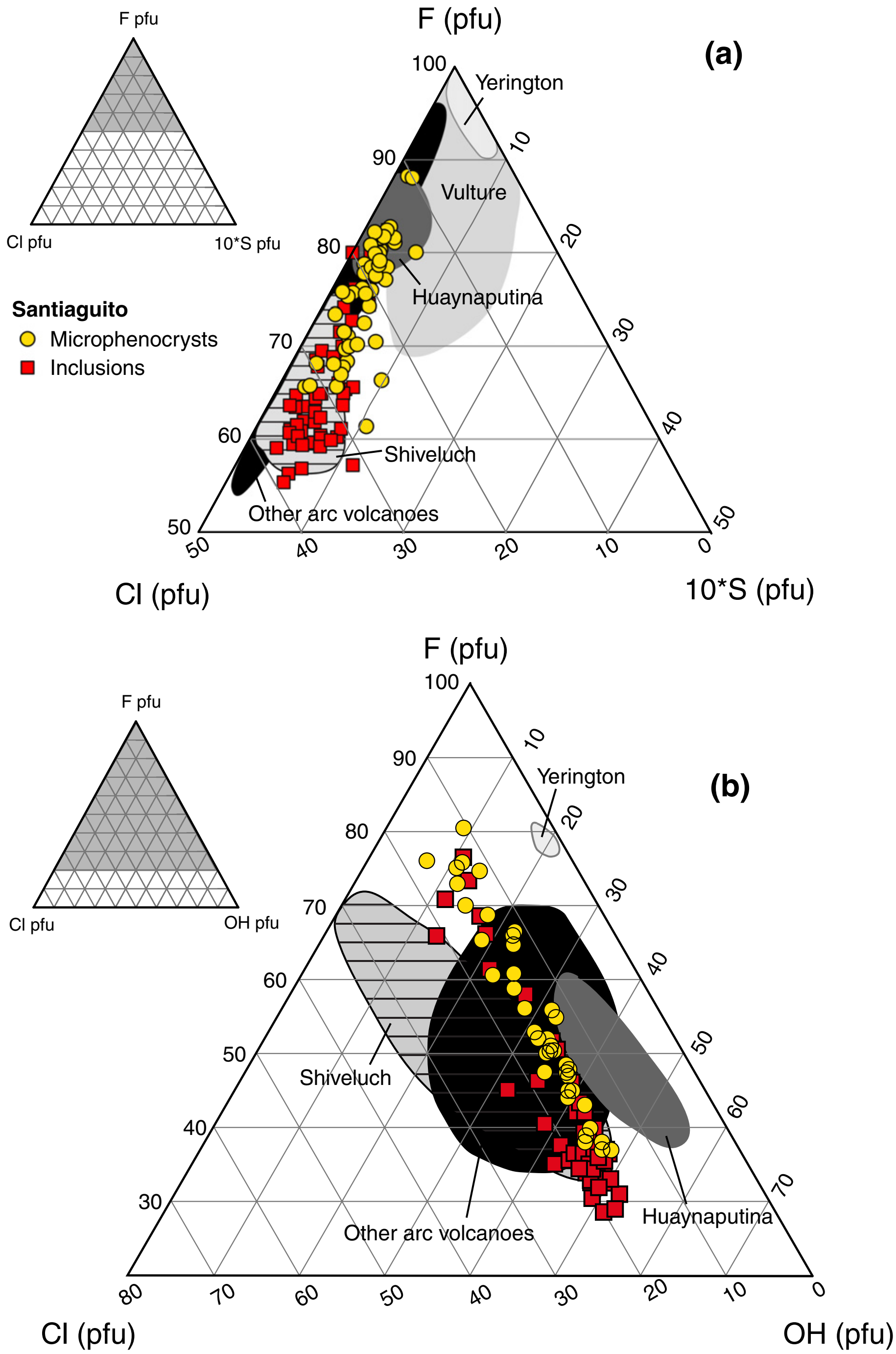

Fig. 3. Ternary diagrams showing (a) S, F, Cl and (b) F, Cl, OH volatile compositions of apatite inclusions (squares) and microphenocrysts (circles) from Santiaguito, expressed as ions per formula unit, with sulphur contents × 10 for ease of comparison. Also shown are fields for other subduction-related systems: Shiveluch Volcano, Kamchatka (Humphreys et al., 2006b), Huaynaputina, Peru (Dietterich and de Silva, 2010), Monte Vulture, Italy (Liu and Comodi, 1993) and Yerington batholith (Streck and Dilles, 1998). 'Other arc volcanoes' (black field) are as reported in Webster et al. (2009), and comprise Krakatau, Indonesia; Pinatubo, Philippines; Mt St Helens, Washington; Santorini, Greece; Lascar, Chile; and Bishop Tuff, California. Insets highlight in grey the sections shown in the main figures.

abundant apatite inclusions in phenocryst phases including plagioclase, pyroxene and Fe-Ti oxides, which suggests that apatite saturation occurred relatively early. This is also supported by the lack of significant P_2O_5 enrichment in the bulk rock compositions (generally < 0.25 wt% P_2O_5, see Scott et al., 2013). We therefore assume that $C^{AST}{}_{SiO2}$ and $C^{AST}{}_{P2O5}$ are equivalent to representative bulk rock compositions (~62–65 wt% SiO_2 and 0.21–0.23 wt% P_2O_5, Scott et al., 2013). We also infer from the abundance of apatites included in phenocrysts that X may be rather low, and must certainly be less than ~0.3 (the proportion of phenocrysts observed in the samples on eruption, Scott et al., 2012, 2013). This range of parameter values gives a range of calculated AST = 897–987 °C (with 'preferred' values in the range 897–963 °C, based on the observation of abundant apatite inclusions within phenocrysts including both plagioclase and pyroxene, leading to the assumption that a reasonable upper limit for the magma crystallinity at apatite saturation is $X = 0.15$, i.e., half of that on eruption). These estimates are at the upper end of (or slightly higher than) temperature estimates for the more evolved magmas (e.g. amphibole-plagioclase geothermometry, 840–950 °C, Scott et al., 2012; two-oxide temperatures, 860–885 °C, Andrews, 2014; Singer et al., 2014), and at the lower end of temperature estimates for the basaltic andesite (925–1040 °C, pyroxene and two-oxide thermometry, Singer et al., 2014).

We then used the empirical relationship obtained by Peng et al. (1997) for the El Chichón trachyandesite to determine a partition coefficient for sulphur:

$$\ln D = \frac{21130}{AST(K)} - 16.2 \quad (2)$$

which gives $D_S^{ap\text{-}m}$ of 2.4–6.4 for the 'preferred' apatite saturation temperatures (897–963 °C). These experimental data were acquired at more oxidising conditions (equivalent to the MnO-Mn_3O_4 to MH buffers) than the Santiaguito magma, and at more appropriate fO_2 conditions $D_S^{ap\text{-}m}$ would be slightly reduced, by perhaps a factor of 2 (Peng et al., 1997). In contrast, the strong increase of $D_S^{ap\text{-}m}$ with decreasing temperature (Peng et al., 1997) means that cooling during fractionation would result in increasing S contents of apatite in equilibrium with a melt of constant composition, resulting in reverse zoning.

Using $D_S^{ap\text{-}m}$ of 2.45–6.4, combined with our measured compositions of apatite inclusions (1656 ± 687 ppm) predicts melt sulphur concentrations in the range 151–957 ppm S. Apatite microphenocryst cores (1396 ppm ± 804) give melt concentrations of 92–899 ppm S. In comparison, measured matrix glass concentrations were generally low, <360 ppm S (Table 2). This suggests that the apatite compositions are a reasonable reflection of coexisting melt sulphur compositions, at least if temperatures are in the lower part of our range (leading to higher partition coefficients). Many of the apatites show systematic zoning, commonly with sulphur-poor rims. It seems unlikely that this is a result of changing temperature during crystallisation, as this would require significant heating (to 940–1100 °C) to crystallise apatite with the lowest observed rim S concentrations (~400 ppm) without any change in melt concentration. It is possible that interaction with mafic magma at depth in the volcanic system could cause such a heating effect; however it seems more likely that the apatites may record syn-eruptive sulphur loss related to degassing.

5.4.2. Fluorine and chlorine

To determine Cl and F concentrations in the melt we used empirical partition coefficients determined for hydrous silicic melts (65–71 wt% SiO_2) in equilibrium with melt and a fluid phase at 200 MPa, 900–924 °C and NNO to NNO + 2.1 (Webster et al., 2009). These parameters are a good match for the estimated magma storage conditions at Santiaguito, although true ternary F-Cl-OH exchange coefficients would be more strictly appropriate than apparent partition coefficients. The data of Webster et al. (2009) show that X_F^{ap} increases with increasing F and decreasing Cl concentration in the melt; X_F/X_{Cl} (ap) increases linearly with X_F/X_{Cl} (m), with X_F/X_{Cl} (ap) ranging from 0.26–14.9 (Webster et al., 2009). Their experiments were run at higher Cl contents than the Santiaguito glass, so we only used data from the less Cl-rich experiments that resulted in apatite with ≤ 2 wt% Cl. These give values of apparent $D_F^{ap\text{-}m}$ (calculated as $D = F^{ap}/F^m$) from 12.7–37. For the same experiments, equivalent values of $D_{Cl}^{ap\text{-}m}$ range from 1.0–3.5.

Using mid-range values for apparent partition coefficients $D_F^{ap\text{-}m}$ (D = 25) and $D_{Cl}^{ap\text{-}m}$ (D = 2.25), the apatite microphenocryst compositions indicate melt halogen concentrations in the range 0.06–0.11 wt% F and 0.38–0.53 wt% Cl; apatite inclusions give melt halogen concentrations of 0.04–0.08 wt% F and 0.46–0.60 wt% Cl. Given the full variation in the partitioning data, the possible range of melt concentrations is large, more like 0.04–0.17 wt% F and 0.29–1.19 wt% Cl (Table 3). This range is consistent with the low measured glass F compositions (lower than the detection limit for at ~0.35 wt% F) and suggests that there has not been significant degassing of F during magma ascent and crystallisation. In contrast, melt inclusions have 700–1600 ppm Cl (Balcone-Boissard et al., 2010), which is substantially lower than the concentrations predicted from our apatite compositions; our matrix glasses analyses show even lower Cl contents (Table 2). This result is similar to that of previous studies (e.g. Boyce and Hervig, 2009; Webster et al., 2009), which also found anomalously high apatite-based estimates for pre-eruptive melt Cl (but not F) concentrations when compared to melt inclusions.

It has been suggested previously that a discrepancy between melt inclusion Cl contents and those calculated from apatite could be due to exsolution of a low-density aqueous vapour from a higher density single-phase fluid coexisting with the magma during ascent (Webster et al., 2009). Subsequent segregation of the low density vapour would result in increasing salinity of the remaining saline fluid and re-equilibration of apatite to more Cl-rich compositions (Webster et al., 2009). There is no direct evidence of the presence of a high density

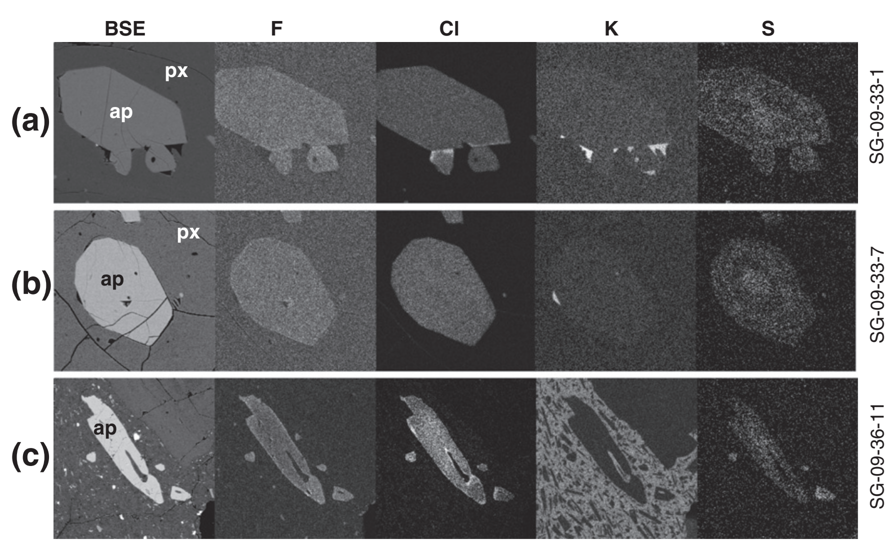

Fig. 4. Back-scattered electron SEM images and X-ray maps showing volatile element zoning in apatite inclusions and microphenocrysts from Santiaguito Volcano. (a) SG-09-33-1, three inclusions in pyroxene host. Small filaments of melt are trapped at the lower margin of the inclusion, clearly visible in the K map. Re-equilibration of apatite Cl contents with the melt is apparent. The inclusion also has a sulphur-rich core. (b) SG-09-33-7, single inclusion within pyroxene host. There is no small-scale re-equilibration as in (a) despite the presence of a small melt pocket, but still clear S-enrichment in the core of the inclusion. (c) SG-09-36-11, microphenocryst with melt embayment. Both F and Cl show clear core-rim zoning, with higher volatile contents at the rim. There is also short lengthscale, high-amplitude zoning in Cl at the rim of the melt embayment. The microphenocryst shows slight S enrichment in the core.

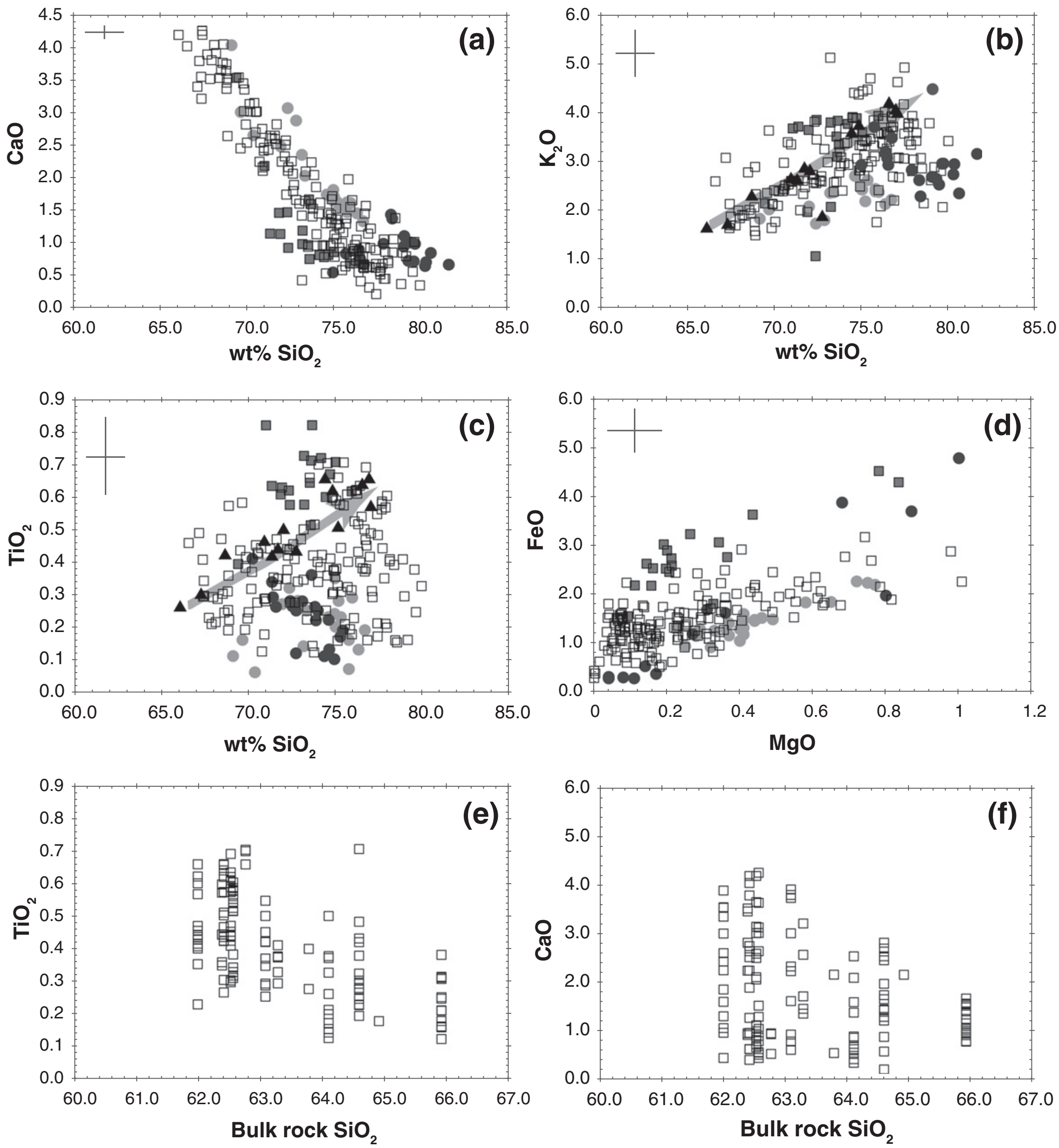

Fig. 5. Glass compositions from Santiaguito Volcano (open squares, matrix glasses from Scott et al., 2013; filled squares, glomerocryst glass from this study) together with published plagioclase-hosted melt inclusion data from the basaltic andesite (dark filled circles) and pumice (light filled circles) of Santa María, 1902 (Singer et al., 2014). Black triangles and underlying grey arrow in (b) and (c) illustrate relatively clear trends seen for individual samples (here, SG-09-03, see Table 2). (a) CaO shows a clear decrease with increasing SiO_2. (b) K_2O contents increase with increasing SiO_2 but the most evolved samples (with ~75 wt% SiO_2) have lower concentrations. (c) TiO_2 shows the same pattern as K_2O but more exaggerated. (d) Good correlation between Fe and Mg contents. (e) and (f). TiO_2 and CaO concentrations decrease with increasing bulk rock SiO_2 content.

saline fluid at Santiaguito, although the melt Cl contents predicted from apatite may be approaching the concentration at which a dense fluid could become stable (Signorelli and Carroll, 2001; Webster, 2004). However, the process described by Webster et al. (2009) should result in partial equilibration of the larger apatite grains to leave Cl-rich rims, whereas Cl-poor rims are observed. It is unlikely that the discrepancy between predicted and observed melt Cl concentrations is the result of apatite growing at volatile-undersaturated conditions, because previous melt inclusion studies demonstrate Cl-H_2O loss during magma ascent (Singer et al., 2014; Villemant et al., 2003). We can also rule out early crystallisation in a higher temperature, less fractionated melt, as this would result in a lower D_{Cl}^{ap-m} (Webster et al., 2009) and hence higher melt Cl contents for a given apatite composition. This leaves the most obvious explanation for the low Cl contents of the matrix glasses being that the matrix has substantially degassed, resulting in loss of Cl into the vapour phase during ascent. This is supported by the covariation of Cl and H_2O in melt inclusions and residual matrix glasses of Plinian clasts (Villemant et al., 2003).

5.5. The 'petrologic method' using apatite

The pre-eruptive dissolved volatile concentrations predicted from apatite can be used to estimate the flux of SO_2, HF, and HCl from Santiaguito, in the same way that the 'petrological method' is commonly used with melt inclusions (e.g. Dietterich and de Silva, 2010; Thordarson et al., 1996; Wallace, 2005). First, the amount of volatiles degassed is constrained using the difference between apatite-based estimates of pre-eruptive melt volatile concentrations (0.29–1.19 wt% Cl, 0.03–0.17 wt% F, 218–676 ppm S, Table 3) and matrix glass volatile concentrations. We use the upper estimates of

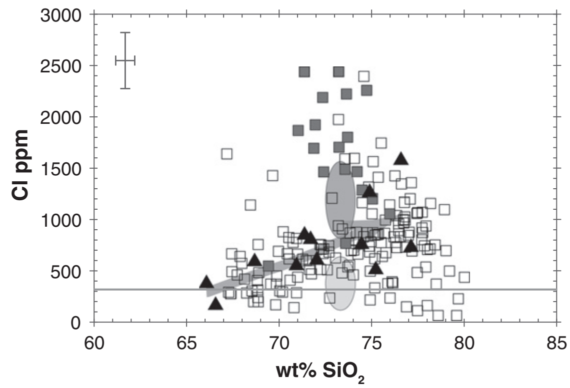

Fig. 6. Cl contents of matrix glasses (open squares) and glomerocryst glasses (filled squares) from Santiaguito Volcano plotted against the SiO_2 content of the host bulk rocks. Cl concentrations follow a similar pattern to K_2O and TiO_2 (see Fig. 5), increasing and then decreasing after ~75 wt% SiO_2. Error bars shows ±1 sigma analytical uncertainty on the analyses; horizontal line represents the detection limit (~300 ppm Cl). Two grey ovals represent the range in composition of matrix glasses and melt inclusions from the 1902 Plinian eruption (dark grey) and later dome rocks (light grey) as measured by electron microprobe (Balcone-Boissard et al., 2010; Villemant et al., 2003).

matrix glass concentrations (0.03 wt% F from Balcone-Boissard et al., 2010; 0.11 wt% Cl and 358 ppm S, Tables 2 and 3) in order to obtain a minimum estimate of the extent of degassing. The total volume of magma erupted at Santiaguito since 1922 is 1.1–2 km^3 (Ebmeier et al., 2012; Harris et al., 2003; Scott et al., 2013); using a typical dacite magma density of 2500 kg m^{-3} gives a total erupted mass of 2.75×10^{12}–5×10^{12} kg. Assuming a mean phenocryst content of ~30% (Scott et al., 2012), this equates to 1.9–3.5×10^{12} kg melt. Thus the total mass of volatiles emitted since 1922 is up to 2.8×10^9 kg S, 2.4×10^9–4.5×10^{10} kg Cl and up to 6.3×10^9 kg F (Table 3).

This suggests time-averaged SO_2 emissions of up to 157 tonnes/ day (Table 3), which is similar to previous estimates based on sporadic field measurements (between 20 and 960 tonnes/day, see Table 4, Andres et al., 1993; Holland et al., 2011; Rodriguez et al., 2004). The same method suggests time-averaged estimates of 74–1380 tonnes/day HCl and up to 196 tonnes/day HF (Table 3). These results give gas species ratios of HF/SO_2 ~ 1.25, and HCl/SO_2 ~ 0.5–8.8. Because the melt Cl concentrations calculated from apatite are rather high compared with melt inclusions (see earlier), we consider that the lower HCl flux values are probably more reliable. There are no published field-based estimates of Santiaguito's halogen emissions, so we are unable to compare this with independent constraints on HCl flux from the volcano. It is not trivial to compare long-term petrological estimates with spot measurements of gas emissions at any individual volcano, primarily because gas fluxes may be highly variable in time, depending on the level of volcanic activity. For example, the HCl flux (and consequently the HCl/SO_2 ratio) at arc volcanoes is typically related to direct magma extrusion and falls to very low levels during periods of non-extrusion (e.g. Edmonds et al., 2001). Spot field measurements for SO_2 at Santiaguito are highly variable in time and also appear to depend on whether there is active extrusion at the lava dome Holland et al., 2011; Rodriguez et al., 2004).

A well-monitored volcanic system that also shows long-term dome-building activity is Soufrière Hills Volcano, Montserrat. Cl is degassed from the andesite magma during extrusion but sulphur is mostly supplied by deeper degassing of unerupted mafic magma (e.g. Edmonds et al., 2001, 2010). Soufrière Hills Volcano has emitted approximately $4.0 \pm 0.6 \times 10^9$ kg sulphur during the course of the prolonged 1995–2011 dome-forming eruption, including both SO_2 and H_2S (Edmonds et al., 2014). Similarly to Santiaguito, SO_2 emission rates have been highly variable during the eruption (e.g. 42 to >1900 tonnes/day during 1996–1997, Young et al., 1998), with long-term time-averaged SO_2 emission rates ~600 tonnes/day SO_2 (Christopher et al., 2010; Edmonds et al., 2014), approximately twice the upper estimate for the SO_2 flux emitted at Santiaguito (see Table 4). At Soufrière Hills Volcano, the HCl/SO_2 ratio is <0.3 during pauses, >1 (up to ~10) during active extrusion (Christopher et al., 2010; Edmonds et al., 2014), with HCl emission rates of >400 tonnes/day during dome-building and <80 tonnes/ day during pauses in extrusion (Edmonds et al., 2002). The inferred HCl flux at Santiaguito is therefore in line with that observed during dome growth at Soufrière Hills. However, the HCl/SO_2 ratios at Santiaguito extend to higher values than Soufrière Hills Volcano. One explanation for this is the apparently substantially lower SO_2 fluxes at Santiaguito. This may reflect differences in the details of the deep plumbing system (a substantial proportion of the SO_2 supply at Soufrière Hills is contributed by unerupted mafic magma, whereas the long-term petrologic estimates for Santiaguito consider only sulphur degassed from the magma that is erupted; alternatively mafic magma

Table 3
Details of "petrologic method" calculations using apatite and matrix glass compositions.

		F wt%		Cl wt%		S, ppm	
		Avg	±1 σ	Avg	±1 σ	Avg	±1 σ
Apatite (microphenocrysts)		1.98	0.45	1	0.11	1396	804
Apatite (inclusions)		1.5	0.46	1.19	0.15	1656	687
Melt, from apatite microphenocrysts[€]*:*							
Calculated melt (using low D[€])		0.166	0.043	1.02	0.17	570	302
Calculated melt (mid-range D)		0.085	0.022	0.453	0.076		
Calculated melt (using high D)		0.057	0.015	0.291	0.049	218	125
Melt, from apatite inclusions[€]*:*							
Calculated melt (using low D)		0.118	0.036	1.19	0.15	676	263
Calculated melt (mid-range D)		0.06	0.018	0.529	0.067		
Calculated melt (using high D)		0.041	0.012	0.34	0.043	259	109
Matrix glass ([*§¶])		0.03		0.083	0.033	135–358	§
Mass degassed, as wt% of melt	min	0		0.126		0	
	max	0.179		1.290		804	
Mass melt erupted since 1922, kg		1.9×10^{12}–3.5×10^{12} (see text for details)					
Mass F, Cl, S degassed, kg	min			2.4E + 09			
	max	6.3E + 09		4.5E + 10		2.81E + 09	
Avg tonnes/day (from 1922–2014)	min			74	HCl		
	max	196	HF	1382	HCl	157	SO2

€ For D values see text.
* Balcone-Boissard et al. (2010) matrix glass concentrations used for F.
§ Most glasses have sulphur bd so use detection limit (135 ppm) as lower limit here. Upper limit is maximum detected concentration (see Table 2).
¶ Average detected matrix glass concentrations used for Cl, Table 2.

Table 4
Estimated volatile flux from Santiaguito, based on apatite analyses (this study), with directly measured flux from other volcanoes for comparison.
Halogen/ SO_2 ratios for Santiaguito were calculated from the petrological data as described in the text.
For Mount St Helens, reported flux data were used to calculate halogen/ SO_2 ratios.
§ SO2 fluxes show short-term variations from 30–154 tonnes/day within individual cycles of explosion and repose.

			SO_2 (tonnes/day)	HF / SO_2 (by mass)	HF (tonnes/day)	HCl / SO_2 (by mass)	HCl (tonnes/day)	References
Santiaguito, Guatemala	This study – petrologic method using apatite and matrix glass		Up to 157	1.25	Up to 196	0.5–8.8	74–1382	
Santiaguito, Guatemala	Persistent degassing, average rates	July 1976 to February 1991	30–210	-	-	-	-	Andres et al. (1993)
	Periods of eruption, average rates	July 1976 to February 1980	60–960	-	-	-	-	Andres et al. (1993)
Santiaguito, Guatemala	Persistent degassing (period of higher lava extrusion rate)	May 2001 to August 2002	20–190	-	-	-	-	Rodriguez et al. (2004)
Santiaguito, Guatemala (§)	Daily average across complete explosion-repose cycles	January 2008–February 2009	55–85	-	-	-	-	Holland et al. (2011)
Fuego, Guatemala	Persistent degassing	May 2001 to August 2002	280–340		-	-	-	Rodriguez et al. (2004)
Pacaya, Guatemala	Persistent degassing	March 1999 to September 2002	350–2380		-	-	-	Rodriguez et al. (2004)
Tacana, Guatemala	Persistent degassing	November 1999	30		-	-	-	Rodriguez et al. (2004)
Popocateptel, Mexico	Dome-building			0.015–0.019		0.11–0.13		Love et al. (1998)
Lascar, Chile	Dome-building			0.16		0.35		Mather et al. (2004)
Mount St Helens, Washington, USA	Dome-building	October 2004 to November 2005	14–240	0.008–0.14	2	0.06–1.0	14	Edmonds et al. (2008), Gerlach et al. (2008)
Soufrière Hills, Montserrat	Dome-building	April 1996 to June 1997	42–1933	0.007	39	0.3–12.6	>400–6000	Allen et al. (2000), Edmonds et al. (2001, 2002), Young et al. (1998)
Sakurajima, Japan	Dome-building			0.009–0.015		0.14–0.33		Mori and Notsu (2003)

supply rates at Santiaguito may differ from those at Soufrière Hills). The mismatch between apatite and melt inclusion Cl contents is another source of uncertainty here.

5.6. Apatite: its potential for tracking volcanic degassing

There is considerable potential for using apatite to infer magmatic volatile contents and time-averaged gas emissions for S, F, and Cl, as an alternative to melt inclusion-based methods (e.g. Huaynaputina, Peru, Dietterich and de Silva, 2010). This may prove particularly useful when direct emissions measurements are unavailable, for historic and prehistoric eruptions, and for comparison with intermittent gas sampling methods, which are typically highly variable in time. However, there still remain significant problems associated with using apatite to infer magmatic volatile concentrations, not least in estimating the point at which apatite started to crystallise. One of the most significant problems is uncertainty over the presence and composition of any fluid(s) coexisting with the melt, coupled with a lack of constraints on the ultimate fate of a brine phase, if present. This uncertainty still exists for melt inclusion studies, but for apatite the problem is trickier because of the strong dependence of apatite halogen contents on fluid composition (Webster et al., 2009). More focus is required on demonstrating possible fluid immiscibility, including documenting the presence of multiple fluid bubbles in melt inclusions, as well as the composition of fluid inclusions. Melt inclusions are useful to constrain whether there has been volatile saturation in the melt.

Additional problems arise when there is also substantial variability in the compositions of apatite. Apatite inclusions and microphenocrysts presented here show considerable compositional variability, with 1 relative standard deviation ~12–15% for Cl, 25–30% for F and 40–50% for S. For the most part this variability appears to be real, although improved precision (e.g. by use of ion microprobe techniques) would be helpful, as would direct analysis of OH for accurate determination of Cl/OH and F/OH ratios. Significant variability between grains means that it is difficult to demonstrate that apatites represent equilibrium compositions, as well as to determine which values are truly representative of pre-eruptive magmatic conditions, and at what conditions. Syn-eruptive diffusive equilibration of microphenocrysts with degassed matrix glass can, in principle, be distinguished from crystallisation effects by considering the lengthscale and anisotropy of compositional gradients. Accurate and precise knowledge of magmatic conditions (fO_2, pressure and temperature) is required for sensible choice of partition coefficients, and thermodynamic calculations may help in this regard. Finally, application of apatite as a tracer of magmatic volatiles would be enhanced by knowledge of partitioning characteristics of all the volatiles (including OH and C), as well as direct determination of these elements in both apatite and melt.

6. Conclusions

The eruption of Santiaguito volcano, Guatemala, is highly active and amongst the longest-lived of its kind in the world. However, due to its location, climate and the surrounding terrain there are few constraints on gas emissions from this volcano. Apatite in Santiaguito lavas retains evidence of volatile zoning, recording loss of sulphur and chlorine between early entrapment of inclusions and crystallisation of microphenocryst rims. This is likely related to degassing of Cl and S from the magma together with aqueous vapour. Pre-eruptive melt volatile concentrations were determined from the apatite compositions using published partition coefficients. These were used, together with matrix glass compositions, to derive time-averaged estimates of SO_2, HF, and HCl fluxes from Santiaguito. These results indicate time-averaged fluxes of up to 157 tonnes/day SO_2, up to 196 tonnes/day HF, and 74–1380 tonnes/day HCl. Estimated ratios are HF/SO_2 ~ 1.25, and HCl/SO_2 0.5–8.8. These fluxes are in line with estimates from other arc volcanoes; however the uncertainties are large and additional work is needed to constrain volatile exchange coefficients between apatite and melt ± fluid(s), including in volatile-undersaturated systems, as well as direct analysis of OH in both apatite and melt.

Supplementary data to this article can be found online at http://dx.doi.org/10.1016/j.lithos.2015.07.004.

Acknowledgements

We acknowledge funding by NERC through PhD studentships NE/G524060/1 (JAJS) and NE/K500811/1 (MJS), standard grant NE/K003852/1, and the NCEO Dynamic Earth and Geohazard group. TAM acknowledges a Royal Society Dorothy Hodgkin fellowship and funding from the Leverhulme Trust. MCSH was supported by a Royal Society University Research fellowship. Sample collection was made possible by Gustavo Chigna, Julio Cornejo, and Jon Stone; older samples were loaned from Bill Rose. We are grateful to both Norman Charnley and Victoria Smith for analytical support. We thank Jim Webster, Adam Simon and Benoit Villemant for helpful review comments that enabled us to improve the manuscript, as well as Nelson Eby for editorial handling.

References

Allen, A.G., Baxter, P.J., Ottley, C.J., 2000. Gas and particle emissions from Soufrière Hills volcano, Montserrat, West Indies: characterization and health hazard assessment. Bulletin of Volcanology 62, 8–19.

Andres, R.J., Rose, W.I., Stoiber, R.E., Williams, S.N., Matias, O., Morales, R., 1993. A summary of sulphur dioxide emission rate measurements from Guatemalan volcanoes. Bulletin of Volcanology 55, 379–388.

Andrews, B.J., 2014. Magmatic storage conditions, decompression rate, and incipient caldera collapse of the 1902 eruption of Santa Maria Volcano, Guatemala. Journal of Volcanology and Geothermal Research 282, 103–114.

Bacon, C.R., 1986. Magmatic inclusions in silicic and intermediate volcanic rocks. Journal of Geophysical Research 91, 6091–6112.

Balcone-Boissard, H., Villemant, B., Boudon, G., 2010. Behavior of halogens during the degassing of felsic magmas. Geochemistry, Geophysics, Geosystems Q09005. http://dx.doi.org/10.1029/2010GC003028.

Blundy, J., Cashman, K., 2001. Ascent-driven crystallisation of dacite magmas at Mount St Helens, 1980–1986. Contributions to Mineralogy and Petrology 140, 631–650.

Bluth, G.J.S., Rose, W.I., 2004. Observations of eruptive activity at Santiaguito volcano, Guatemala. Journal of Volcanology and Geothermal Research 136, 297–302.

Bouvier, A.-S., Metrich, N., Deloule, E., 2008. Slab-derived fluids in the magma sources of St. Vincent (Lesser Antilles arc): Volatile and light element imprints. Journal of Petrology 49, 1427–1448.

Boyce, J.W., Hervig, R.L., 2009. Apatite as a monitor of late-stage magmatic processes at Volcan Irazú, Costa Rica. Contributions to Mineralogy and Petrology 157, 135–145.

Brenan, J., 1994. Kinetics of fluorine, chlorine, and hydroxyl exchange in fluorapatite. Chemical Geology 110, 195–210.

Browne, B.L., Gardner, J.E., 2006. The influence of magma ascent path on the textures, mineralogy and formation of hornblende reaction rims. Earth and Planetary Science Letters 246, 161–176.

Christopher, T., Edmonds, M., Humphreys, M.C.S., Herd, R.A., 2010. Volcanic gas emissions from Soufriere Hills Volcano, Montserrat 1995–2009, with implications for mafic magma supply and degassing. Geophysical Research Letters 37, L00E04.

Devine, J.D., Sigurdsson, H., Davis, A.N., Self, S., 1984. Estimates of sulfur and chlorine yield to the atmosphere from volcanic eruptions and potential climatic effects. Journal of Geophysical Research 89, 6309–6325.

Devine, J.D., Gardner, J.E., Brack, H.P., Layne, G.D., Rutherford, M.J., 1995. Comparison of microanalytical methods for estimating H_2O contents of silicic volcanic glasses. American Mineralogist 80, 319–328.

Dietterich, H., de Silva, S., 2010. Sulfur yield of the 1600 eruption of Huaynaputina, Peru: contributions from the magmatic, fluid-phase, and hydrothermal sulfur. Journal of Volcanology and Geothermal Research 197, 303–312.

Doherty, A.L., Webster, J.D., Goldoff, B.A., Piccoli, P.M., 2014. Partitioning behavior of chlorine and fluorine in felsic melt-fluid(s)-apatite systems at 50 MPa and 850–950 °C. Chemical Geology 384, 94–111.

Ebmeier, S.K., Biggs, J., Mather, T., Elliott, J., Wadge, G., Amelung, F., 2012. Measuring large topographic change with InSAR: Lava thicknesses, extrusion rate and subsidence rate at Santiaguito volcano, Guatemala. Earth and Planetary Science Letters 335–336, 216–225.

Edmonds, M., Pyle, D., Oppenheimer, C., 2001. A model for degassing at the Soufrière Hills volcano, Montserrat, West Indies, based on geochemical data. Earth and Planetary Science Letters 186, 159–173.

Edmonds, M., Pyle, D., Oppenheimer, C., 2002. HCl emissions at Soufrière Hills volcano, Montserrat, West Indies, during a second phase of dome-building: November 1999 to October 2000. Bulletin of Volcanology 64, 21–30.

Edmonds, M., McGee, K.A., Doukas, M.P., 2008. Chlorine degassing during the lava dome-building eruption of Mount St Helens, 2004–2005. US Geological Survey Professional Paper 1750, 572–589.

Edmonds, M., Aiuppa, A., Humphreys, M., Moretti, R., Giudice, G., Martin, R.S., Herd, R.A., Christopher, T., 2010. Excess volatiles supplied by mingling of mafic magma at an andesite arc volcano. Geochemistry, Geophysics, Geosystems 11 (4), Q04005.

Edmonds, M., Humphreys, M.C.S., Hauri, E., Herd, R.A., Wadge, G., Rawson, H., Ledden, R., Plail, M., Barclay, J., Aiuppa, A., Christopher, T., Giudice, G., Guida, R., 2014. Pre-eruptive vapour and its role in controlling eruption style and longevity at Soufriere Hills Volcano. In: Wadge, G., Robertson, R., Voight, B. (Eds.), The eruption of Soufriere Hills Volcano, Montserrat from 2000–2010Geological Society of London Memoir 39, 291–315.

Erdmann, S., Martel, C., Pichavant, M., Kushnir, A., 2014. Amphibole as an archivist of magmatic crystallization conditions: problems, potential, and implications for inferring magma storage prior to the paroxysmal 2010 eruption of Mount Merapi, Indonesia. Contributions to Mineralogy and Petrology 167, 1016.

Escobar Wolf, R., Matías Gomez, R.O., Rose, W.I., 2010. Notes on a New Geologic Map of Santiaguito Dome Complex, Guatemala. Geological Society of America Digital Map and Chart Series 8. http://dx.doi.org/10.1130/2010.DMCH008 (2 pp.).

Gerlach, T.M., McGee, K.A., Doukas, M.P., 2008. Emission rates of CO_2, SO_2, and H_2S, scrubbing, and pre-eruption excess volatiles at Mount St Helens, 2004–2005. US Geological Survey Professional Paper 1750, 543–571.

Goldoff, B., Webster, J.D., Harlov, D.E., 2012. Characterization of fluor-chlorapatites by electron probe microanalysis with a focus on time-dependent intensity variation of halogens. American Mineralogist 97, 1103–1115.

Harris, A.J.L., Rose, W.I., Flynn, L.P., 2003. Temporal trends in lava dome extrusion at Santiaguito 1922–2000. Bulletin of Volcanology 65, 77–89.

Holland, A.S.P., Watson, I.M., Phillips, J.C., Caricchi, L., Dalton, M.P., 2011. Degassing processes during lava dome growth: insights form Santiaguito lava dome, Guatemala. Journal of Volcanology and Geothermal Research 202, 153–166.

Holness, M.B., Humphreys, M.C.S., Sides, R., Helz, R.T., Tegner, C., 2012. Toward an understanding of disequilibrium dihedral angles in mafic rocks. Journal of Geophysical Research 117, B06207.

Humphreys, M.C.S., Kearns, S.L., Blundy, J.D., 2006a. SIMS investigation of electron-beam damage to hydrous, rhyolitic glasses: Implications for melt inclusion analysis. American Mineralogist 91, 667–679.

Humphreys, M.C.S., Blundy, J.D., Sparks, R.S.J., 2006b. Magma evolution and open-system processes at Shiveluch volcano: insights from phenocryst zoning. Journal of Petrology 47, 2303–2334.

Humphreys, M.C.S., Blundy, J.D., Sparks, R.S.J., 2008. Shallow-level decompression crystallization and deep magma supply at Shiveluch volcano. Contributions to Mineralogy and Petrology 155, 45–61.

Jicha, B.R., Smith, K.E., Singer, B.D., Beard, B.L., Johnson, C.M., Rogers, N.W., 2010. Crustal assimilation no match for slab fluids beneath Volcan de Santa Maria, Guatemala. Geology 38, 859–862.

Liu, Y., Comodi, P., 1993. Some aspects of the crystal-chemistry of apatites. Mineralogical Magazine 57, 709–719.

Love, S.P., Goff, F., Counce, D., Siebe, C., Delgado, H., 1998. Passive infrared spectroscopy of the eruption plume at Popocatépetl volcano, Mexico. Nature 396, 563–566.

Martin, R.S., Mather, T.A., Pyle, D.M., Watt, S.F.L., Day, J.A., Collins, S.J., Wright, T.E., Aiuppa, A., Calabrese, S., 2009. Sweet chestnut (Castanea sativa) leaves as a bio-indicator of volcanic gas, aerosol and ash deposition onto the flanks of Mt Etna in 2005–2007. Journal of Volcanology and Geothermal Research 179, 107–119.

Mather, T.A., Tsanev, V.I., Pyle, D.M., McGonigle, A.J.S., Oppenheimer, C., Allen, A.G., 2004. Characterization and evolution of tropospheric plumes from Lascar and Villarrica volcanoes, Chile. Journal of Geophysical Research – Atmospheres 109, D21303.

Mori, T., Notsu, K., 2003. Ground-based remote FT-IR measurements of volcanic gas chemistry at Sakurajima volcano, Japan. Geochimica et Cosmochimica Acta 67, A304.

Parat, F., Holtz, F., 2004. Sulfur partitioning between apatite and melt and effect of sulfur on apatite solubility at oxidizing conditions. Contributions to Mineralogy and Petrology 147, 201–212.

Parat, F., Holtz, F., 2005. Sulfur partition coefficient between apatite and rhyolite: the role of bulk S content. Contributions to Mineralogy and Petrology 150, 643–651.

Peng, G., Luhr, J.F., McGee, J.J., 1997. Factors controlling sulfur concentrations in volcanic apatite. American Mineralogist 82, 1210–1224.

Piccoli, P., Candela, P., 1994. Apatite in felsic rocks: a model for the estimation of initial halogen concentrations in the Bishop Tuff (Long Valley) and Tuolumne intrusive suite (Sierra Nevada batholith) magmas. American Journal of Science 294, 92–135.

Piccoli, P., Candela, P., 2002. Apatite in igneous systems. Reviews in Mineralogy and Geochemistry 48, 255–292.

Ridolfi, F., Renzulli, A., Puerini, M., 2010. Stability and chemical equilibrium of amphibole in calc-alkaline magmas: an overview, new thermobarometric formulations and applications to subduction-related volcanoes. Contributions to Mineralogy and Petrology 160, 45–66.

Robock, A., 2000. Volcanic eruptions and climate. Reviews of Geophysics 38, 191–219.

Rodriguez, L.A., Watson, I.M., Rose, W.I., Branan, Y.K., Bluth, G.J.S., Chigna, G., Matias, O., Escobar, D., Carn, S., Fischer, T., 2004. SO_2 emissions to the atmosphere from active volcanoes in Guatemala and El Salvador. Journal of Volcanology and Geothermal Research 138, 325–344.

Rose, W.I., 1972. Santiaguito volcanic dome, Guatemala. Geological Society of America Bulletin 83, 1413–1434.

Rose, W.I., 1987. Santa María, Guatemala: bimodal soda-rich calc-alkalic stratovolcano. Journal of Volcanology and Geothermal Research 33, 109–129.

Sahetapy-Engel, S.T.M., Flynn, L.P., Harris, A.J.L., Bluth, G.J., Rose, W.I., Matias, O., 2004. Surface temperature and spectra measurements at Santiaguito lava dome, Guatemala. Geophysical Research Letters 31, L19610.

Scott, J.A.J., 2012. Origin and evolution of the Santiaguito lava dome complex, Guatemala. Unpublished PhD thesis, University of Oxford, 400 pp.

Scott, J.A.J., Mather, T.A., Pyle, D.M., Rose, W.I., Chigna, G., 2012. The magmatic plumbing system beneath Santiaguito volcano, Guatemala. Journal of Volcanology and Geothermal Research 237–238, 54–68.

Scott, J.A.J., Pyle, D.M., Mather, T.A., Rose, W.I., 2013. Geochemistry and evolution of the Santiaguito volcanic dome complex, Guatemala. Journal of Volcanology and Geothermal Research 252, 92–107.

Signorelli, S., Carroll, M.R., 2001. Experimental constraints on the origin of chlorine emissions at the Soufrière Hills volcano, Montserrat. Bulletin of Volcanology 62, 431–440.

Singer, B.D., Smith, K.E., Jicha, B.R., Beard, B.L., Johnson, C.M., Roger, N.W., 2011. Tracking open-system differentiation during growth of Santa María Volcano, Guatemala. Journal of Petrology 52, 2335–2363.

Singer, B.S., Jicha, B.R., Fournelle, J.H., Beard, B.L., Johnson, C.M., Smith, K.E., Greene, S.E., Kita, N.T., Valley, J.W., Spicuzza, M.J., Rogers, N.W., 2014. Lying in wait: deep and shallow evolution of dacite beneath Volcan de Santa María, Guatemala. In: Gomez-Tuena, A., Straub, S.M., Zellmer, G.F. (Eds.), Orogenic Andesites and Crustal GrowthGeological Society, London, Special Publications 385, 209–234.

Stock, M.J., Humphreys, M.C.S., Smith, V.C., Johnson, R.D., Pyle, D.M., 2015. Apatite as magmatic volatile probe: quantifying the mechanisms and rates of EPMA-induced halogen migration. American Mineralogist 100, 281–293.

Stormer Jr., J.C., Pierson, M.L., Tacker, R.C., 1993. Variation of F and Cl x-ray intensity due to anisotropic diffusion in apatite during electron microprobe analysis. American Mineralogist 78, 641–648.

Streck, M.J., Dilles, J.H., 1998. Sulfur evolution of oxidized arc magmas as recorded in apatite from a porphyry copper batholith. Geology 26, 523–526.

Suetsugu, Y., Takahashi, Y., Okamura, F.P., Tanaka, J., 2000. Structure analysis of A-type carbonate apatite by a single-crystal X-ray diffraction method. Journal of Solid State Chemistry 155, 292–297.

Thordarson, Th., Self, S., Oskarsson, N., Hulsebosch, T., 1996. Sulfur, chlorine and fluorine degassing and atmospheric loading by the 1783–1784 AD Laki (Skaftar Fires) eruption in Iceland. Bulletin of Volcanology 58, 205–225.

Villemant, B., Boudon, G., Nougrigat, S., Poteaux, S., Michel, A., 2003. Water and halogens in volcanic clasts: tracers of degassing processes during Plinian and dome-building eruptions. In: Oppenheimer, C., Pyle, D.M., Barclay, J. (Eds.), Volcanic degassing. Geological Society, London, Special Publications 213, 63–79.

Wallace, P.J., 2005. Volatiles in subduction zone magmas: concentrations and fluxes based on melt inclusion and volcanic gas data. Journal of Volcanology and Geothermal Research 140, 217–240.

Webster, J.D., 2004. The exsolution of magmatic hydrosaline chloride liquids. Chemical Geology 210, 33–48.

Webster, J.D., Tappen, C.M., Mandeville, C.W., 2009. Partitioning behaviour of chlorine and fluorine in the system apatite-silicate melt-fluid. II: felsic silicate systems at 200 MPa. Geochimica et Cosmochimica Acta 72, 559–581.

Wyllie, P.J., Cox, K.G., Biggar, G.M., 1962. The habit of apatite in synthetic and igneous systems. Journal of Petrology 3, 238–243.

Young, S.R., Francis, P.W., Barclay, J., Casadevall, T.J., Gardner, C.A., Darroux, B., Davies, M.A., Delmelle, P., Norton, G.E., Maciejewski, A.J.H., Oppenheimer, C.M.M., Stix, J., Watson, I.M., 1998. Monitoring SO_2 emissions at the Soufrière Hills volcano: implications for changes in eruptive conditions. Geophysical Research Letters 25, 3681–3684.